



## **Final Draft**

### **of the original manuscript**

Bouali, A.; André, N.; Silva Campos, M.; Serdechnova, M.; Dos Santos, J.; Amancio-Filho, S.; Zheludkevich, M.:

**Influence of LDH conversion coatings on the adhesion and corrosion protection of friction spot-joined AA2024-T3/CF-PPS.**

In: Journal of Materials Processing Technology. Vol. 67 (2021) 197 – 210.

First published online by Elsevier: 26.07.2020

<https://dx.doi.org/10.1016/j.jmst.2020.06.038>

# Influence of LDH conversion coatings on the adhesion and corrosion protection of friction spot-joined AA2024-T3/CF-PPS

A.C. Bouali<sup>a\*</sup>, N.M. André<sup>b</sup>, M.R. Silva Campos<sup>a</sup>, M. Serdechnova<sup>a</sup>, J.F. dos Santos<sup>b</sup>, S.T. Amancio-Filho<sup>c</sup>, M.L. Zheludkevich<sup>a,d</sup>

<sup>a</sup> Institute of Materials Research, Helmholtz-Zentrum Geesthacht, Magnesium Innovation Center, Corrosion and Surface Technology, Max-Planck-Straße 1, 21502 Geesthacht, Germany.

<sup>b</sup> Institute of Materials Research, Helmholtz-Zentrum Geesthacht, Materials Mechanics, Solid State Joining Processes, Max-Planck-Straße 1, 21502 Geesthacht, Germany.

<sup>c</sup> Graz University of Technology – TU Graz, Institute of Materials Science, Joining and Forming, BMVIT Endowed Professorship for Aviation, Kopernikusgasse 24/1, 8010 Graz – Austria

<sup>d</sup> Faculty of Engineering, University of Kiel, Kaiserstrasse 2, 24143 Kiel, Germany

## Abstract

Layered double hydroxide (LDH) conversion coatings loaded with corrosion inhibitors were suggested for the surface treatment of the aluminum alloy 2024-T3, prior to friction spot joining with carbon-fiber reinforced polyphenylene sulfide (AA2024-T3/CF-PPS). Vanadate was used as a model corrosion inhibitor. Lap shear testing method revealed an increase of 15 % of the joint's adhesion performance when treated with LDH and before exposure to salt spray. The evaluation of the joints after exposure to salt spray demonstrated a significant difference in the corrosion behavior of the joints when the AA2024-T3 is treated with LDH loaded with nitrate and vanadate species. The LDH intercalated with nitrate revealed a clear improvement on the mechanical and corrosion resistance performance of the joints, even after 6 weeks of salt spray. However, the LDH intercalated with vanadate failed in providing protection against corrosion as well as preserving the mechanical properties of the joints. The effect of the galvanic corrosion was further investigated by zero resistance ammeter measurements as well as localized scanning vibrating electrode technique.

**Keywords:** Friction spot joining, layered double hydroxide, galvanic couple, corrosion protection, adhesion

\* Corresponding author: Tel. /Fax: +49 4152 87-1943/ 1960 email: anissa.bouali@hzg.de

## 35 **I. Introduction**

36 Every year, the transportation industry spends a considerable amount of money in repairing  
37 damages related to corrosion. Among the various types of corrosion that raise concern is the  
38 galvanic corrosion or dissimilar metal corrosion [1]. Knowing that nowadays, many structures  
39 rely on a multi-material assembly due its high technological and economic benefits, the need  
40 for a solution to counter the problem of galvanic corrosion is a priority for industrial  
41 applications.

42 Carbon-fiber reinforced polymers (CFRPs) are being largely used especially in aircraft industry  
43 owing to their higher specific strength and stiffness over those of conventional metal alloys [2],  
44 besides they are electrically conductive and relatively inert [3, 4]. Therefore, they are often a  
45 material of choice when it comes to their joining with other metals such as Al alloys.  
46 Nevertheless, several issues were encountered during and after the process of joining a metal  
47 with a polymer composite material, some of which are the formation of bubbles and generation  
48 of gaps at the interface between the metal and polymer. These issues can lead to a decrease of  
49 joint mechanical properties and their fast degradation [5]. Several investigations were devoted  
50 to countering these issues. Most proposed solutions include a change on the configuration of  
51 the joining methodology [5-8] and/or surface pre-treatment of the parts [8-13]. Both solutions  
52 contributed in reinforcing the mechanical interlocking between the metal and composite and  
53 strengthen the adhesion of the joints. In the case of surface pre-treatment, the aim was not only  
54 to improve the adhesion and mechanical performance of the joints but also in some cases to  
55 minimize their corrosion degradation [5, 10].

56 CFRPs have a more noble potential compared to most metals. As a result, when galvanically  
57 coupled with aluminum alloys, the CFRP serves as the cathode supporting oxygen reduction  
58 and the aluminum alloy serves as the anode where accelerated dissolution takes place by  
59 galvanic action [3, 4]. According to the different relevant methods of joining (chemical,  
60 mechanical or welding) aluminum alloy with CFRPs, several studies have been conducted to  
61 understand and overcome the issue of galvanic corrosion [4, 14-22].

62 M. Mandel and L. Krüger [19] investigated the evolution of the pitting corrosion susceptibility  
63 of the EN AW-6060-T6 aluminum alloy on the self-piercing rivet joint with CFRP. The long-  
64 term analysis was achieved by a combination of climate chamber and salt spray test along with  
65 electrochemical evaluation by polarization measurements. The Al alloy potentiodynamic  
66 polarization curves revealed a passive region followed by a transpassive one. Galvanic coupling  
67 with CFRP shifts the corrosion potential of the structure to the transpassive region for aluminum  
68 alloy and induces the localized corrosion.

69 In another study, a comparable galvanic effect of AA7075-T6 and AA1050 when coupled with  
70 carbon fiber composite was shown by Z. Liu et al. [20]. Indeed, using zero resistance ammeter  
71 (ZRA) as the main investigation technique, the authors reported a higher coupling current  
72 density for AA1050 compared to AA7075-T6. It was stated that the intermetallic associated  
73 with AA7075-T6 alloy reduces the galvanic effect when coupled with the composite.

74 A prevalent method that is often used to mitigate galvanic corrosion, is to insulate the concerned  
75 parts (e.g. Al alloys and CFRP) to avoid their direct contact, hence maintaining the electric  
76 contact only by means of a third part which can be a metallic fastener [4]. In this respect, R.  
77 Srinivasan, J.A. Nelson and L.H. Hihara [4] evaluated the efficiency of inserting a fiberglass  
78 insulative skirt (with various lengths) between the mechanically coupled AA6061-T6 and CFR-  
79 PMCs (Carbon fiber reinforced polymer-matrix composites). Based on a set of experimental  
80 data supported with modelling and calculations, they proposed an interesting model which  
81 relates the galvanic corrosion rate to the following ratio: insulating skirt length/salt loading.  
82 This aims to enable the design of a proper skirt length to attenuate galvanic corrosion, by taking  
83 into account the salt-loading levels on the environment. More recently, L. Pan et al. [22] utilized  
84 a different procedure that relies on coating of AA5083 sheets with a polyaniline modified epoxy  
85 adhesive before bond-riveted joining with carbon-fiber reinforced polymers. The reported  
86 electrochemical results and single lap shear testing, showed an improvement of the corrosion  
87 resistance of the joints with a minimal influence on the mechanical properties of the rivets.

88 An alternative methodology to tackle the problematic of galvanic corrosion is to introduce  
89 corrosion inhibitors. In this frame, many interesting results were achieved [16, 23-25] such as  
90 the ones demonstrated by S. Kallip et al. [16]. The authors exploited the synergistic combination  
91 of 1,2,3-benzotriazole (BTA) and  $Ce(NO_3)_3$  to efficiently inhibit the galvanic corrosion  
92 resulting from the couple Zn/Fe. This same inhibitor combination was utilized by L.B. Coelho  
93 et al. [23] for the corrosion inhibition of the galvanic couple Al/Cu. In latter work, the inhibitive  
94 effect of the combination BTA +  $Ce(NO_3)_3$  was analyzed using the scanning vibrating electrode  
95 technique (SVET) assisted with further analysis by UV spectrophotometry and ToF-SIMS. It  
96 was confirmed that a formation of a mixed BTA-based /Cerium based film took place on the  
97 Cu surface interfering with the corrosion reaction. This work was followed a short time after  
98 by another work where a similar inhibitive effect using cerium chloride and triethanolamine on  
99 graphite - AA2024-T3 galvanic couple was demonstrated [24]. Two main conclusions were  
100 drawn from the previous study; first, cerium ions act preferentially as inhibitors for the localized  
101 corrosion of AA2024-T3 when coupled with graphite, whereas the triethanolamine inhibition  
102 mechanism relies on the formation of complexes with the Cu-rich intermetallic. Secondly, the

103 inhibition mechanism is highly dependent on the electrode's cathode to anode ratio. For  
104 instance, cerium ions failed to provide an efficient corrosion inhibition at a high cathodic/anodic  
105 ratio due to the strong anodic activity of the AA2024-T3 induced by the important macro-  
106 galvanic effect [24].

107 The strategy of using corrosion inhibitors for the purpose of attenuating galvanic corrosion is  
108 well-known, however these additives need to be added in a manner to ensure a targeted and  
109 controlled inhibition. Thus, many other studies proposed the implementation of a carrier that  
110 could transport the corrosion inhibitors into the targeted area in a controlled manner [17, 26-  
111 28]. This role of carrier is often fulfilled by layered double hydroxide (LDH) nanocontainers  
112 [17, 26-28]. LDH consists of a stacking of brucite-like sheets formed of octahedral ( $M^{2+}$ ,  
113  $M^{3+}$ )(OH)<sub>6</sub> that share common edges [29-30]. The partial substitution of the divalent cations by  
114 trivalent cations generates an excess of positive charge that is balanced by the presence of  
115 anions between the interlayers together with water molecules [31-32]. These anions between  
116 the interlayers can be swapped by active species such as corrosion inhibitors. This confers to  
117 LDH two main roles; i) to capture aggressive ions such as chlorides, and ii) to carry the  
118 inhibitors and release them when activated by different triggers (pH, presence of corrosion  
119 species etc.). Interesting results were achieved in this direction especially for the corrosion  
120 protection of aluminum alloys [28, 33-35]. Among these results are the ones reported by J.  
121 Tedim et al. [28], where a novel Zn-Al LDH functional layer was prepared directly on the  
122 AA2024 surface, through a conversion reaction with the metal. The self-healing properties of  
123 the LDH was demonstrated after intercalation of vanadate as corrosion inhibitor. This same  
124 group performed further investigation of the LDH film preparation and tested several  
125 parameters to provide an optimized and efficient corrosion protection to AA2024-T3 [34].  
126 These LDH films were also next analyzed by SVET and EIS and have displayed efficient  
127 localized corrosion protection for the AA2024-T3 substrate [35].

128 In the course of this work, we propose a follow-up to a previous investigation carried out on a  
129 galvanic couple AA2024-T3/CF-PPS joined by friction spot joining (FSpJ) method. In the  
130 previous study, the authors performed a thorough investigation of the corrosion behavior of the  
131 joints. The microstructural changes on the AA2024-T3, induced by the FSpJ process led to  
132 inhomogeneities on the corrosion behavior with a preferential corrosion of the heat affected  
133 zone (HAZ). The overall corrosion of AA2024-T3 was further intensified by macro-galvanic  
134 effect as a result of its coupling with CF-PPS. The polarization curves indicated an  $E_{\text{couple}} = -$   
135  $0.52$  V and  $I_{\text{couple}} = 19$   $\mu\text{A}/\text{cm}^2$  for the system AA2024-T3/CF-PPS [36].

136 Herein, we aim to counter the galvanic corrosion of the couple AA2024-T3/CF-PPS by putting  
137 forward an approach based on Zn-Al LDH conversion coatings directly produced on the  
138 AA2024-T3 alloy. Two LDH conversion layers will be prepared, one intercalated with nitrate  
139 and a second with vanadate (model corrosion inhibitor). The influence of the Zn-Al LDH films  
140 on the mechanical performance of the final joints will be investigated. Next, a systematic  
141 evaluation of the corrosion performance of the respective joints is performed using general and  
142 localized techniques.

## 143 **II. Materials and methods**

### 144 **2.1. Materials**

#### 145 *2.1.1. Test specimens*

146 The aluminum alloy 2024-T3 was provided by Constellium (France) [37], its nominal  
147 composition in wt. % is: 4.55 Cu, 0.17 Fe, 1.49 Mg, 0.45 Mn, 0.10 Si, 0.02 Ti, 0.16 Zn, less  
148 than 0.01 Cr and Al balance.

149 The carbon-fiber reinforced polyphenylene sulfide (CF-PPS) was purchased from TenCate  
150 (Netherlands) [38]. This specific CF-PPS laminate is composed of 43 % carbon fibers. This  
151 quasi-isotropic laminate composite consists of seven carbon-fiber fabric reinforcement plies in  
152 the [(0.90)/(±45)]<sub>3</sub>/(0.90) sequence.

153 The dimensions of the parts are 100 mm x 25.4 mm with nominal thickness of 2 mm and 2.17  
154 mm for the AA2024-T3 and CF-PPS sheets, respectively.

#### 155 *2.1.2. Chemicals*

156 For the synthesis of the Zn-Al LDH conversion coatings, the following chemicals were used:  
157 zinc nitrate hexahydrate ( $\text{Zn}(\text{NO}_3)_2 \cdot 6\text{H}_2\text{O}$ , >99%, Alfa Aesar, Germany), ammonium nitrate  
158 ( $\text{NH}_4\text{NO}_3$ , >99%, Acros Organics, Germany), ammonia solution ( $\text{NH}_3 \cdot \text{H}_2\text{O}$ , 25%, Merck  
159 KGaA, Germany), sodium vanadate oxide ( $\text{NaVO}_3$ , 96%, Alfa Aesar, Germany). Deionized  
160 water was used for the preparation of the solutions and the cleaning process.

### 161 **2.2. Samples preparation**

#### 162 *2.2.1. Sandblasting*

163 Sandblasting allows to manually clean the AA2024-T3 surface and to enhance the adhesive  
164 strength of the joints by modifying its surface roughness [36,39].

165 Aluminum oxide ( $\text{Al}_2\text{O}_3$ ) dry particles with an average size of 100 to 150  $\mu\text{m}$  were used for the  
166 sandblasting procedure. The sandblasting of the aluminum took place from a distance of 20 cm  
167 with an incident angle of 45°. The procedure was performed for 10 s and a final average surface  
168 roughness of  $6.8 \pm 0.3 \mu\text{m}$  was reached. After the sandblasting the specimens were cleaned in  
169 ultrasonic water bath and dried with pressurized air.

170 **2.2.2. LDH treatment**

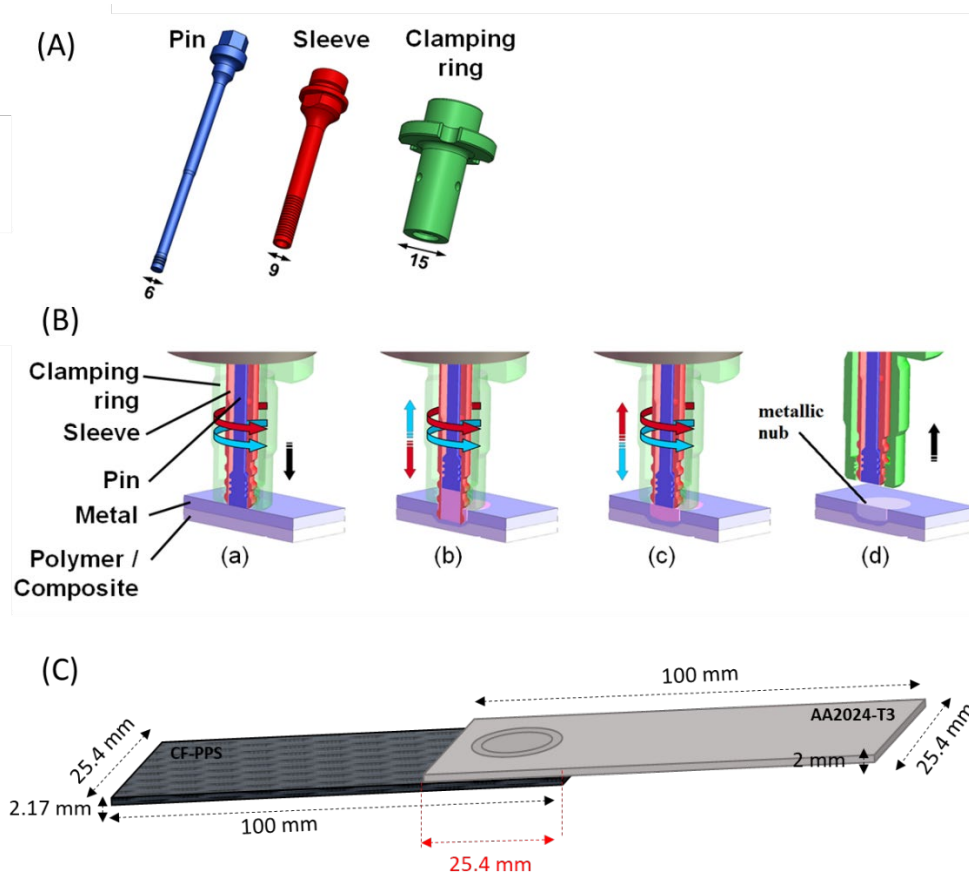
171 In order to produce the Zn-Al-NO<sub>3</sub> LDH-based conversion layer, a solution containing 0.1 M  
172 of Zn (NO<sub>3</sub>)<sub>2</sub> and 0.6 M of NH<sub>4</sub>NO<sub>3</sub> was prepared and adjusted to a neutral pH with 1 wt. %  
173 NH<sub>3</sub>·H<sub>2</sub>O solution. The AA2024-T3 samples were immersed for 30 min at 95 °C with  
174 continuous stirring [28]. The samples were then rinsed with deionized water and dried at room  
175 temperature.

176 Part of the AA2024-T3 plates coated with Zn-Al LDH-NO<sub>3</sub> were subjected to an anion  
177 exchange reaction with vanadate by simple immersion in a solution containing 0.1 M NaVO<sub>3</sub>  
178 for 30 min at 50°C. The samples were rinsed with deionized water and dried at room  
179 temperature.

180 **2.2.3. Production of the joints**

181 After the LDH treatment of the AA2024-T3 parts, they were joined to CF-PPS by Friction Spot  
182 Joining (FSpJ). The AA2024-T3/CF-PPS joints were produced using an RPS 200 (Harms &  
183 Wende, Germany) joining equipment mounted with a non-consumable tool consisting of three  
184 parts (clamping ring, sleeve and pin) to generate frictional heat (**Fig. 1-A**).

185  
186



187

188 **Fig. 1.** (A) Tool used to produce the samples (dimensions in mm), (B) Steps of the FSpJ process: (a)  
189 overlapping of parts and tool, (b) plunging of the sleeve into the metal, (c) keyhole refilling with  
190 plasticized metal, and (d) joint consolidation (Adapted from [40]), (C) dimension of the final joint.

## 191 **2.3.Characterization**

### 192 **2.3.1. Surface observation and analysis**

193 The surface appearance and elemental composition of the specimens prior to the joining by  
194 FSpJ process, as well as after the mechanical testing and separation by lap shear test, were  
195 analyzed using a Tescan Vega3 SB scanning electron microscope (SEM, Brno, Czech Republic)  
196 equipped with an *eumeX* energy dispersive X-ray (EDS, Heidenrod, Germany) spectrometer.

197 The X-ray diffraction patterns for the specimens were collected with a Bruker D8 Advance  
198 diffractometer (Karlsruhe, Germany) using a Cu K $\alpha$  target as a radiation source. The  
199 measurement was done with an incident angle of 3°, step size was 0.02° and the dwell time was  
200 equal to 1 s. For further calculation regarding the LDH structure, the 2 $\theta$  scan range employed  
201 was from 5° to 65°.

202 Raman spectroscopy point analysis was also conducted using a Confocal Raman microscope  
203 (Bruker Senterra II, Ettlingen, Germany). The following parameters were utilized to obtain the  
204 spectra: wavelength of 532 nm, laser power of 50 mW and an aperture of 50  $\mu$ m.

### 205 **2.3.2. Mechanical test**

206 The influence of the LDH treatment on the mechanical performance of the joints was evaluated  
207 using a universal testing machine Zwick/Roell 1478 (Germany) according to the ASTM  
208 standard D 3163 (lap shear testing). The tests were performed before and after exposure to salt  
209 spray (SST), at room temperature with a cross-head speed of 1.27 mm/min. For the mechanical  
210 test, at least 3 replicates for every sample type were used.

### 211 **2.3.3. Corrosion investigation**

212 As a first step, general and localized electrochemical tests in the form of zero resistance  
213 ammeter (ZRA) measurements and scanning vibrating electrode technique (SVET), were  
214 carried out to evaluate the possible electrochemical processes involved during corrosion.

215 ZRA was used in order to estimate the galvanic current and the mixed potential of the couple  
216 AA2024-T3/CF-PPS. This was done on an Interface 1000E Potentiostat/galvanostat/ZRA  
217 (Gamry, USA) monitored with a Gamry framework system. In these terms, both AA2024-T3  
218 and CF-PPS were the working electrodes and the reference electrode was silver/silver chloride

219 (Ag/AgCl). The measurements lasted for 25 h and were achieved at room temperature in a  
220 solution of 0.5 % NaCl with continuous stirring at 200 rpm.

221 The SVET device employed for this work is from Applicable Electronics Inc. (New Haven,  
222 USA) and is controlled with ASET-LV4 software from Science Wares (Falmouth,  
223 Massachusetts, USA). A homemade cell composed of an embedded AA2024-T3 rod and a  
224 CFRP rod (65% Tenax HT 24 K carbon fiber in an epoxy vinyl matrix) separated by a distance  
225 of 0.6 mm was built to carry out the measurement. The cell set-up is similar to the one used in  
226 a previous study (see **Fig. S.1 a** in supplementary material) [41]. An electrical wire was used to  
227 connect both rods during the measurement. It is important to mention that the composite CFRP  
228 rod used for the SVET investigation is different to the composite CF-PPS used in the rest of the  
229 study. The reason being that for the SVET measurements, specific dimensions were needed to  
230 build up the cell and the dimension of this CFRP rod were the most suitable.

231 The measurements were performed in a 0.05 M NaCl solution using a Pt/Ir vibrating probe with  
232 a tip that was platinized to form a sphere with an average diameter of 15  $\mu\text{m}$ . The SVET probe  
233 was maintained at a distance of 100  $\mu\text{m}$  from the surface. An image illustrating the final set-up  
234 is shown in **Fig. S.1 b**.

235 The scanning area was around 7000 x 3000  $\mu\text{m}^2$  with a step size of 80 x 50. The final obtained  
236 data was reconstructed into maps using the free Quickgrid program.

237  
238 The second step of the study was to subject the different AA2024-T3/CF-PPS joints (bare,  
239 LDH-NO<sub>3</sub>-treated and LDH-VO<sub>x</sub>-treated AA2024-T3) to a salt spray test (SST) according to  
240 the ASTM B1177-16 standard. The joints were placed in a chamber at an angle of 30°. The  
241 temperature of the chamber was maintained at 35°C and the pressure was of 1 bar. A  
242 concentration of 5 % NaCl was used for the salt fog. Three replicates from every sample type  
243 were taken in order to verify the reproducibility of the results.

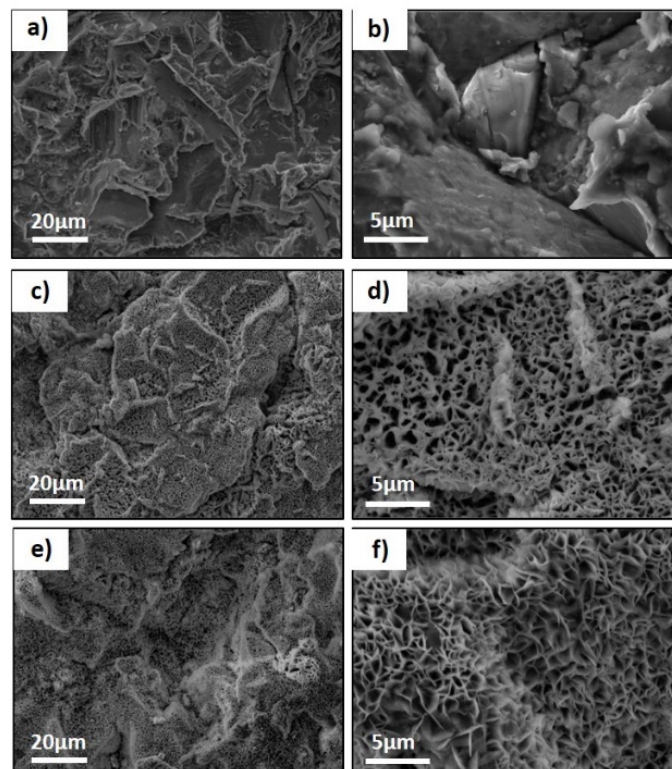
244

### 245 **III. Results**

#### 246 **3.1. Surface structure and morphology before FSpJ**

247 Prior to joining with the CF-PPS parts, the morphology of the different treated AA2024-T3  
248 plates were observed with SEM (**Fig. 2**). The sandblasted AA2024-T3 surface micrographs are  
249 showed in **Fig. 2 a** and **b**. The sandblasting with Al<sub>2</sub>O<sub>3</sub> particles resulted in surface irregularities  
250 in form of crests and valleys that are more pronounced in some regions than others. After LDH  
251 treatment, the micrographs (**Fig. 2 c** and **d**) reveal a compact, flake-like structure film that  
252 covers the whole sample surface, following the morphology of the original surface

253 (sandblasted). The overall appearance of the LDH film does not change after undergoing anion-  
254 exchange reaction with the model corrosion inhibitor (vanadate) (**Fig. 2 e and f**). The previous  
255 described features were further analyzed with EDS. The resulting selective elemental maps for  
256 Al, Zn, N, V and O are illustrated in the supplementary material (**Fig. S.2**). The reference  
257 AA2024-T3 without any treatment is mainly enriched in Al and O (**Fig. S.2 a**). After formation  
258 of LDH-NO<sub>3</sub>, the analysis indicated an enrichment in Zn and N in addition to Al and O (**Fig.**  
259 **S.2 b**). This suggests that the formed LDH-NO<sub>3</sub> film is primarily composed of these elements.  
260 A homogeneous distribution of the element V appeared after anion-exchange with vanadate,  
261 according to the results depicted on **Fig. S.2 c**.

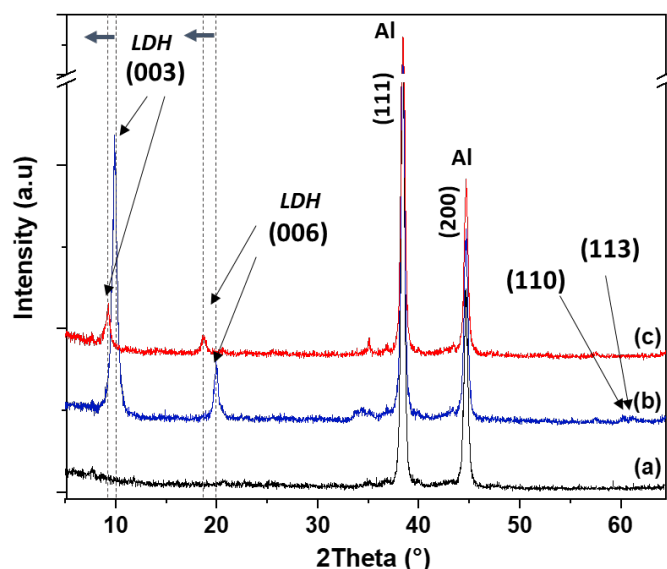


262

263 **Fig. 2.** SEM micrographs of sandblasted AA2024-T3 without LDH treatment a) and b); with LDH-  
264 NO<sub>3</sub> c) and d); with LDH-VO<sub>x</sub> e) and f).

265

266 The EDS results can indicate whether the supposed interlayer anions (NO<sub>3</sub><sup>-</sup> and VO<sub>x</sub><sup>n-</sup>) are  
267 present, but it does not attest of their successful intercalation between the LDH layers. For this  
268 purpose, X-ray diffraction investigation was performed and the obtained patterns are depicted  
269 in **Fig. 3**.



270  
 271 **Fig. 3.** XRD pattern of sandblasted AA2024-T3 without LDH treatment a); with LDH-NO<sub>3</sub> b); with  
 272 LDH-VO<sub>x</sub> c).  
 273

274 The pattern in **Fig. 3 a** belongs to the AA2024-T3 samples without any treatment, and it shows  
 275 two typical reflections (111) and (200) associated with the Al substrate. In addition to the (111)  
 276 and (200) reflections, the XRD pattern of AA2024-T3 treated with LDH-NO<sub>3</sub> (pattern **(b)**) show  
 277 typical LDH-NO<sub>3</sub> reflections which are related to the basal planes (003) at 9.8° and (006) at  
 278 19.8°. At higher 2θ angles, the non-basal peaks for (110) and (113) can be identified [42]. After  
 279 intercalation of vanadate (pattern **(c)**), the position of the basal peaks for (003) and (006) shift  
 280 to the left side to 9.3° and 18.7° respectively. The reason behind this shift can be attributed to  
 281 the expansion of the LDH interlayer spacing, to host the vanadate anion that is bigger in size in  
 282 comparison to the nitrate anion [32, 43-44].  
 283

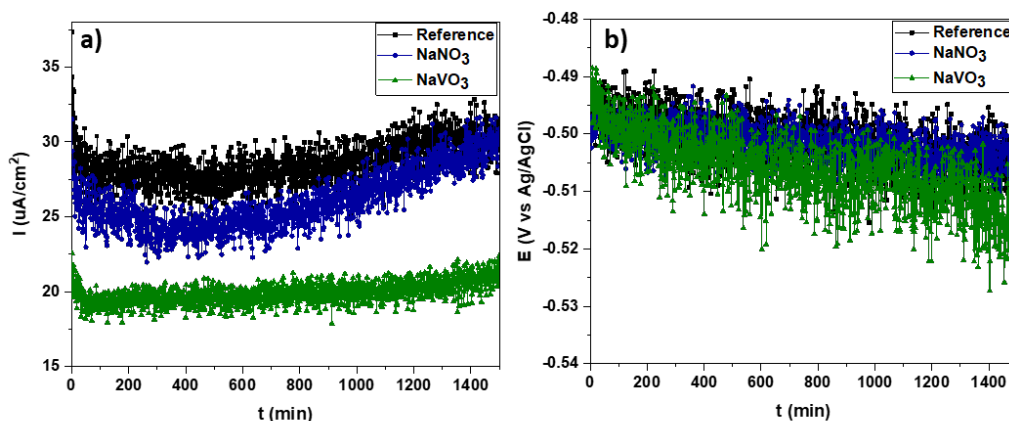
### 284 **3.2. Electrochemical characterization**

285 Zero resistance ammeter (ZRA) is a method that can be used for monitoring the current flowing  
 286 between two galvanically coupled materials [45]. The mixed potential of galvanic can also be  
 287 monitored at the same time. The graphical output of the experiment is a plot of current and  
 288 potential versus time (**Fig. 4**).

289 For this part of the study, it was of interest to understand whether the species NO<sub>3</sub><sup>-</sup> and VO<sub>x</sub><sup>n-</sup>  
 290 would contribute to the overall reduction of corrosion.

291 The current density measured between AA2024-T3 and CF-PPS is represented in **Fig. 4 a** and  
 292 the mixed potential between these two parts in **Fig. 4 b**. The curves in **Fig. 4 a** and **b** account

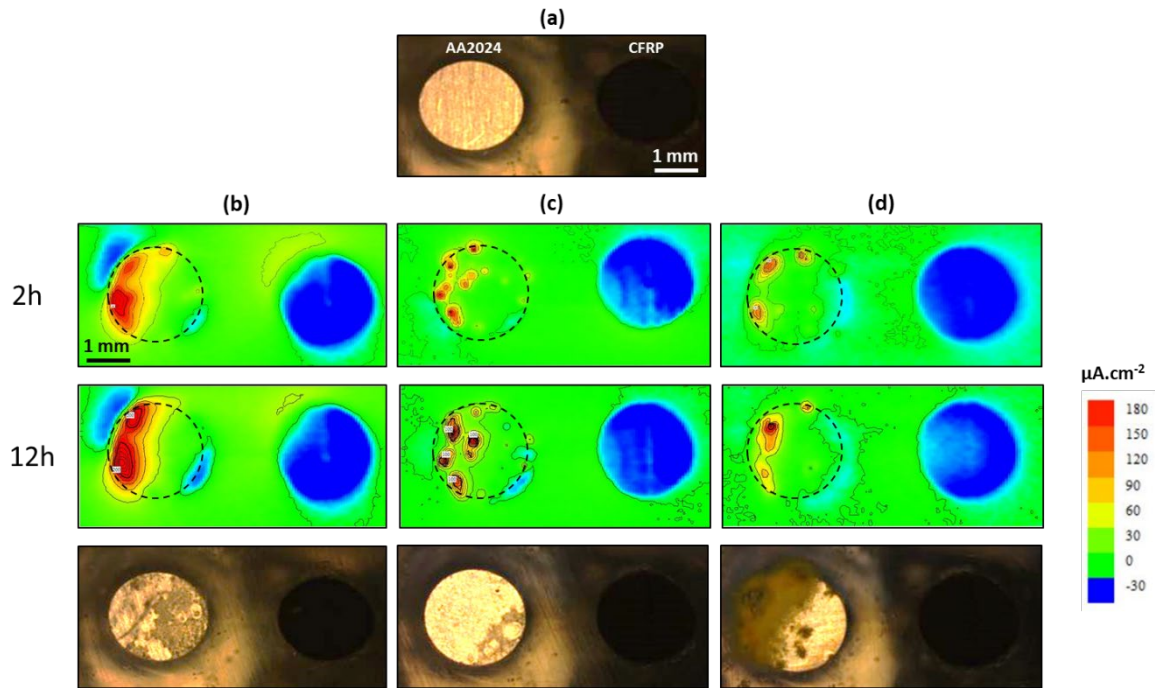
293 for the behavior of the couple AA2024-T3/CF-PPS when directly exposed to a solution of 0.5  
294 % NaCl (0.5 % NaCl corresponds approx. to 0.085 M NaCl); 0.5 % NaCl +  $10^{-3}$  M NaNO<sub>3</sub> and  
295 0.5 % NaCl +  $10^{-3}$  M NaVO<sub>3</sub>. Herein, the evaluation of the performance of the active agents  
296 ( $\text{NO}_3^-$  and  $\text{VO}_x^{n-}$ ) solely, is achieved.



297  
298 **Fig. 4.** Galvanic corrosion measurements of the galvanic couple AA2024-T3/CF-PPS at different  
299 conditions; with a) representing the current density and b) mixed potential between AA2024-T3 and  
300 CF-PPS when exposed to 0.5 % NaCl, 0.5 % NaCl +  $10^{-3}$  M NaNO<sub>3</sub> and 0.5 % NaCl +  $10^{-3}$  M NaVO<sub>3</sub>.

301  
302 From **Fig. 4**, it can be observed that the samples exposed to the solution containing  $10^{-3}$  M  
303 NaVO<sub>3</sub> shows the lowest galvanic current in comparison to the ones exposed to  $10^{-3}$  M NaNO<sub>3</sub>  
304 and to the reference electrolyte. This suggests that the presence of NaVO<sub>3</sub> contributes to the  
305 reduction of the anodic activity of AA2024-T3. Indeed, considering the fact that the CF-PPS  
306 surface is not altered, the decrease of the galvanic current density suggests that the galvanic  
307 corrosion is not controlled anymore solely by the oxygen diffusion to the cathodic electrode.  
308 The decrease of the anodic reaction rate contributes also to the measured current and to the rate  
309 of the galvanic corrosion. The results also clearly demonstrate a corrosion inhibition effect of  
310 vanadate present in the electrolyte. However, the inhibition efficiency after 25 hours is not high  
311 ( $\sim 32\%$ ) in comparison to the inhibition efficiency previously reported for uncoupled AA2024  
312 [46-47]. A large spatial separation of cathodic and anodic zones can be one of the factors  
313 contributing to the observed effect. Moreover, the ZRA measurements do not account for the  
314 cathodic processes taking place on the local micro-cathodes on the surface of the AA2024-T3.  
315 Therefore, SVET was used in this work to monitor the evolution of local current densities on  
316 anodes and cathodes using the model galvanic cell described above (**Fig. S.1**). A micrograph  
317 of the galvanic couple is also shown in **Fig. 5 a**.

318 Similarly to ZRA, the model galvanic cell was exposed to three different electrolytes: a solution  
 319 of 0.05 M NaCl, 0.05 M NaCl +  $10^{-3}$  M NaNO<sub>3</sub> and 0.05M NaCl +  $10^{-3}$  M NaVO<sub>3</sub>. The  
 320 concentration of NaCl is a standard generally used for SVET measurements [48]. Moreover,  
 321 the additional  $10^{-3}$  M of the other salts (NaNO<sub>3</sub> and NaVO<sub>3</sub>) are too low to have any influence  
 322 on the overall resistivity of the electrolyte (resistivity fixed after calibration) [41].

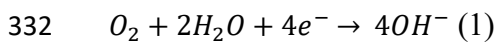


323  
 324

325 **Fig. 5.** a ) Optical micrograph of the cell at  $t=0$ ; SVET maps of the coupled system (AA2024-  
 326 T3/CFRP) after 2h and 12h immersion followed by an optical micrograph of the cell at the different  
 327 solutions of b) 0.05M NaCl, c) 0.05M NaCl +  $10^{-3}$  M NaNO<sub>3</sub> and d) 0.05M NaCl +  $10^{-3}$  M NaVO<sub>3</sub>.

328

329 The CFRP side of the maps form in every scenario (**Fig. 5 b-d**) a nearly perfect cathodic circle,  
 330 which is expected, due to the high oxygen reduction reactions (ORR) taking place on its surface  
 331 according to Equation 1 [49].



333 A severe anodic activity is discerned on the AA2024-T3 side of the reference system with only  
 334 0.05 M NaCl (**Fig. 5 b**) and seems to intensify after 12 h immersion. Well defined cathodic  
 335 activities can be also noted at the edges of the AA2024-T3 part. This implies that alongside  
 336 macro-galvanic corrosion due to the coupling with the CFRP rod, micro-galvanic corrosion as  
 337 a result of the presence of micro-galvanic cells between the intermetallic phases in the AA2024-  
 338 T3 (e.g. Al<sub>2</sub>CuMg, Al<sub>2</sub>Cu) and the Al matrix, also contributes to the overall corrosion processes  
 339 taking place at the interface of the AA2024-T3.

340 The addition of sodium nitrate to the electrolyte leads to the appearance of small spread  
341 localized anodic areas on AA2024. Nevertheless, the overall anodic activity is reduced. Few  
342 local pits with high anodic current densities appear on the surface (**Fig. 5 c**) in contrast to nitrate-  
343 free electrolyte, where larger anodic areas are evidenced (**Fig. 5 a**).

344  
345 In the system with 0.05 M NaCl +  $10^{-3}$  M NaVO<sub>3</sub>, a major decline of the corrosion activity can  
346 be noted even after 12 h immersion (**Fig. 5 d**). Another interesting observation is the formation  
347 of a yellowish layer on one side of the AA2024-T3 (see photograph **Fig. S.3**). It can be seen  
348 that this layer is mainly present on the area where pitting attacks take place (according to the  
349 maps of 2h and 12h) and generally pitting is induced by the presence of Cu-rich intermetallic  
350 [50]. This yellowish layer has been associated with the formation of a vanadate protective layer,  
351 that can impede corrosion processes by displacement of oxygen and chloride from the AA2024-  
352 T3 surface [46-47]. Moreover, the reduction of vanadate takes place preferentially at Cu-rich  
353 intermetallic, hence explaining the strong vanadate adsorption in this area of the Al alloy [46-  
354 47, 51].

355 For the sake of comparison, additional SVET measurements were performed with the same  
356 systems but by disconnecting the AA2024-T3 rod from the CFRP. The idea is to study the  
357 corrosion behavior of AA2024-T3 by excluding the macro-galvanic effect resulting from the  
358 coupling with CFRP. The results are depicted in the supplementary materials **Fig. S.4**.

359 The first remark that can be made from the SVET maps in **Fig. S.4** is that the CFRP side (right  
360 side of the maps) remains completely inert, no activity was recorded. This response is awaited  
361 as the CFRP is not activated by coupling with AA2024-T3. Another important feature concerns  
362 the magnitude of the current densities. The anodic current densities recorded for the uncoupled  
363 system ( $\sim 10 \mu\text{A}\cdot\text{cm}^{-2}$ ) are much lower than those of the coupled system ( $\sim 200 \mu\text{A}\cdot\text{cm}^{-2}$ ). This  
364 confirm once more the severity of AA2024-T3 corrosion when it is subjected to galvanic  
365 coupling with CFRP.

366 The maps on **Fig. S.4 a** and **b** show noticeable anodic activities on the AA2024-T3  
367 accompanied by more pronounced cathodic activities as a result of oxygen reduction reactions.  
368 No amelioration can be distinguished with the solution containing NaNO<sub>3</sub>.

369 The most relevant results were obtained with the system in the presence of 0.05 M NaCl +  
370  $10^{-3}$  M NaVO<sub>3</sub>. A halo of cathodic activity appears on the AA2024-T3 side with a complete  
371 absence of anodic activity. Besides, when looking at the micrograph following the 12 h  
372 immersion, no degradation can be seen on the surface of the AA2024-T3 especially when  
373 compared to the micrographs of the two other systems. It cannot be denied that the vanadate

374 suppressed the corrosion processes at the interface of AA2024-T3, but the mechanism  
375 governing the inhibition action is unlike the mechanism that occurred for the coupled system  
376 (**Fig. 5 d**). Indeed, no adsorbed layer was formed in this particular event.

377 The reason behind this operating mode of vanadate must probably be associated with its  
378 property to exist in various forms. And this depends highly on factors such as the pH and the  
379 oxidation state. It has been suggested in the literature that metals such as Al based alloys have  
380 strong reducing capabilities, hence they could easily accelerate the decomposition of some  
381 vanadate species (e.g. reduction of monovanadate ) and this cathodic process do not always  
382 lead to the formation of a protective film on the AA2024-T3 interface [46]. Moreover, as this  
383 process may be dominant in **Fig. S.4**, the anodic activity is still present but concealed and the  
384 SVET was able to only detect the high cathodic currents. Similar reduction reaction of vanadate  
385 may have also occurred on the coupled system (**Fig. 5**), but the associated current densities  
386 were probably within the noise level of the experiment.

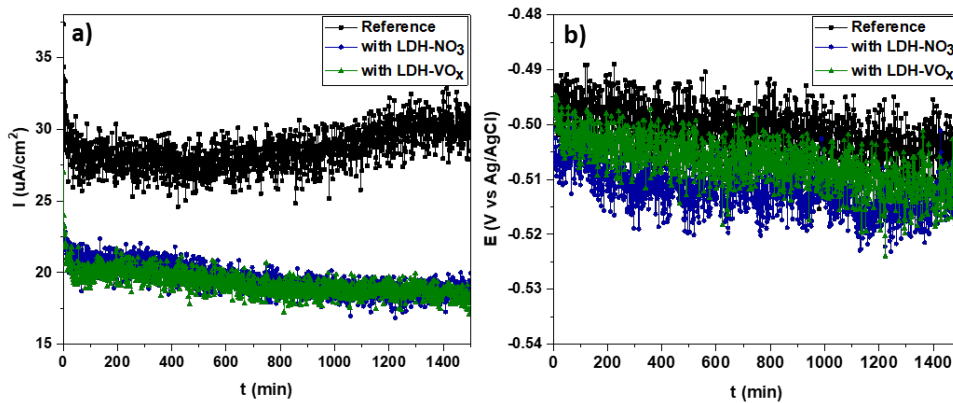
387

388 On one hand, the ZRA and SVET measurements above allowed to understand how the  
389 AA2024-T3/CF-PPS galvanic couple would behave in the presence of nitrate and vanadate  
390 anions. On the other hand, the collected information does not provide enough insight on the  
391 impact of these same anions when loaded into the LDH conversion films.

392 On that account, AA2024-T3 with no treatment; AA2024-T3 with LDH-NO<sub>3</sub> and AA2024-T3  
393 with LDH-VO<sub>x</sub> were subjected to a galvanic corrosion assessment facing CF-PPS in a solution  
394 of 0.5 % NaCl. By doing so, we can determine the influence of the LDH conversion coatings  
395 loaded with the respective inhibitors, on the overall galvanic corrosion. The results of the ZRA  
396 investigation in shown in **Fig. 6**.

397 For the purpose of clarification, the following denomination was given to the different  
398 specimens: AA2024-T3/CF-PPS refers to the reference joint, AA2024-T3-LDH-N/CF-PPS is  
399 the AA2024-T3 sample treated with LDH-NO<sub>3</sub> and joined with CF-PPS and finally AA2024-  
400 T3-LDH-V/CF-PPS that consist of the AA2024-T3 sample treated with LDH-VO<sub>x</sub> and joined  
401 with CF-PPS.

402



403

404 **Fig. 6.** ZRA measurement representing a) the current density and b) the mixed potential between the  
 405 reference AA2024-T3, AA2024-T3-LDH-N and AA2024-T3-LDH-V when coupled with CF-PPS and  
 406 exposed to 0.5 % NaCl solution.

407 As it can be seen from **Fig. 6**, the values of the current density (**Fig. 6 a**) and potential (**Fig. 6**  
 408 **b**) fall into the same range as the ones registered for the measurements performed in the  
 409 electrolyte containing the nitrate and vanadate species (**Fig 4**). The potential curves for the  
 410 different samples in each case are close to one another. The current density curves of the  
 411 samples AA2024-T3 with LDH-NO<sub>3</sub> and LDH-VO<sub>x</sub> coupled with CF-PPS are overlapped  
 412 meaning that they present similar behavior. Moreover, their respective galvanic current  
 413 densities are lower in comparison to the reference couple AA2024-T3/CF-PPS.

414 The presence of LDH treatment on the surface of AA2024 leads to a moderate decrease of the  
 415 galvanic current. This suggests that the conversion treatment can suppress the anodic activity  
 416 on the alloys surface. Moreover, when comparing the behavior of the AA2024-T3-LDH-V  
 417 coupled with CF-PPS (green curves - **Fig. 6**) and the curves obtained with AA2024-T3/CF-PPS  
 418 immersed in a solution of 0.05 M NaCl + 10<sup>-3</sup> NaVO<sub>3</sub> (green curves - **Fig. 4**), it can be seen that  
 419 the current density and potential values for both experiments fall in the same range. Therefore,  
 420 it can be assumed that the encapsulation of vanadate in to the LDH layers do not obstruct their  
 421 function of corrosion inhibition.

422

### 423 3.3. Overview after FSpJ and exposure to SST

#### 424 3.3.1. Macro visual examination of the joints

425 Following the results of the electrochemical evaluation, salt spray test was used as a second  
 426 step in the corrosion investigation. The FSp joints were placed inside the SST chamber  
 427 simulating a corrosive environment according to ASTM B117-16. A superficial first inspection  
 428 of the joints was achieved by a comparison of photographs taken at predetermined periods  
 429 before and after exposure to SST. The photographs are disclosed in **Fig. 7**.

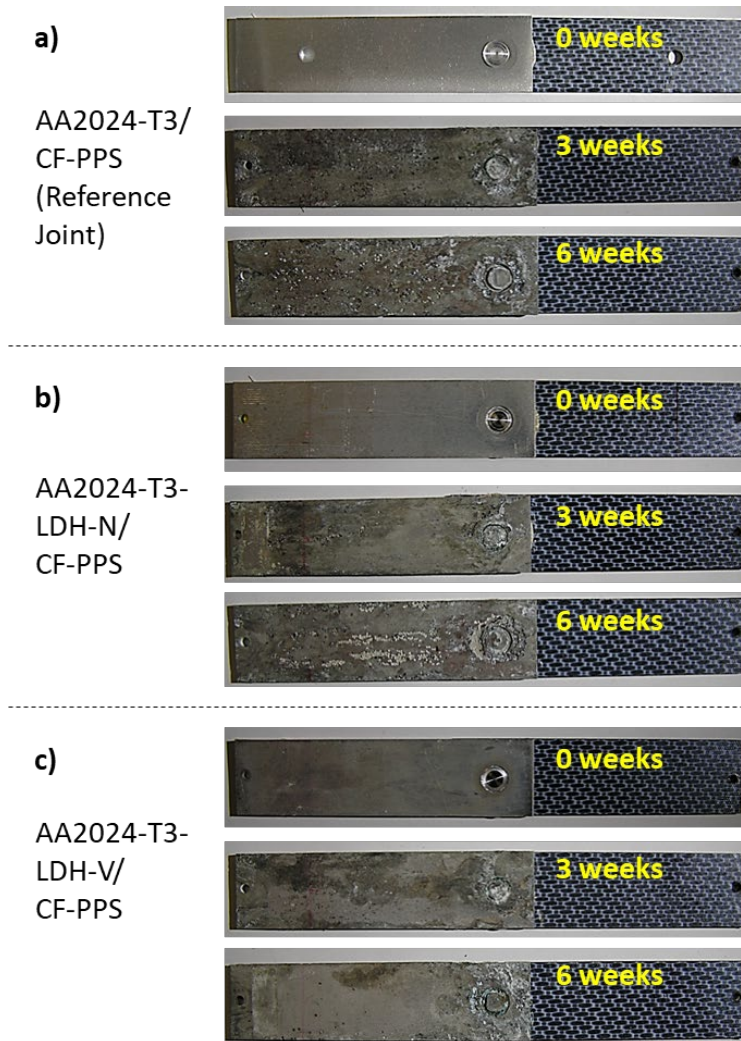


**Fig. 7.** Photographs of the joints taken before and after 3 weeks and 6 weeks exposure to SST.

430  
431  
432  
433

434 After 3 weeks of SST exposure, a substantial localized corrosion can be noted along the  
435 AA2024-T3 surface outside the joint and at the nugget zone of the AA2024-T3 part. This  
436 aggravates further after 6 weeks SST (**Fig. 7 a**). The system with LDH-nitrate demonstrated a  
437 better behavior after 3 weeks SST in comparison to the reference. However, after 6 weeks SST,  
438 degradation by pitting corrosion also occurs which led to the formation of a network of  
439 corrosion pits in the middle of the upper surface (**Fig. 7 b**).

440 An improvement can be noticed with the AA2024-T3-LDH-V/CF-PPS (**Fig. 7 c**) showing  
441 almost no localized corrosion attacks on the interface outside the joining area. This confirms an  
442 active corrosion protection achieved via corrosion inhibition by the vanadate released from the  
443 LDH conversion layers. However, the localized corrosion can be still evidenced around the  
444 joining area and at the nugget zone. This confirms that vanadate is an efficient corrosion  
445 inhibitor in the cases where macro-galvanic coupling is absent, otherwise the inhibition

446 efficiency is not sufficient to guarantee a long-term protection. Therefore, at longer distances  
447 from the joint, where the galvanic effect is much lower because of IR drop through the thin  
448 electrolyte film, the inhibition is efficient. At proximity of CF-PPS, strong pitting attacks is  
449 noticed. This attack seems to be even stronger in the case of vanadate containing system than  
450 for other samples. This is because the anodic activity on the AA2024-T3-LDH-V/CF-PPS is  
451 not spread along large surface areas, but is rather concentrated in local zones causing deep  
452 pitting. The partial removal of the LDH-VO<sub>x</sub> conversion layer in the nugget zone due to the  
453 high shear forces applied during the FSpJ process, could also explain the concentrated corrosion  
454 degradation in these zones.

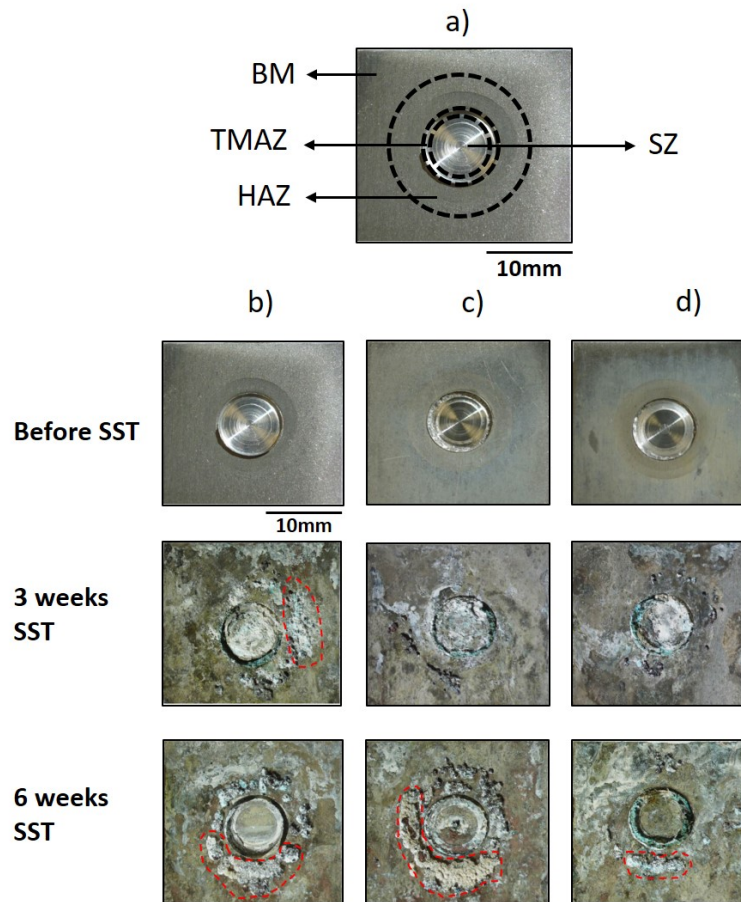
455 Photographs of nugget zone of all systems exposed for different times to SST are shown in **Fig.**  
456 **8**. The interaction between the FSpJ tool and the AA2024-T3 leading to the generation of  
457 frictional heat and the increase of temperature, induces an important alteration on the internal  
458 microstructure of the AA2024-T3 around the area. Four main microstructural regions can be  
459 recognized as a result of the process (**Fig. 8 a**) [36, 39]; the metal stir zone (SZ), located in the  
460 center of the joining area, is subject to the highest heat generation and peak temperatures. The  
461 thermo-mechanically affected zone (TMAZ), is also influenced by high temperatures and  
462 severe metal deformation as a result of the tool's rotational speed and frictional actions.  
463 The zone between the TMAZ and the base material (BM) is called the metal heat affected zone  
464 (HAZ).

465 At first glance to the photographs of the specimens after exposure to SST, it can already be seen  
466 that the different described zones (SZ, TMAZ, HAZ and BM) respond to corrosion in a very  
467 distinct manner. A number of concise studies have reported similar findings, so as to the  
468 microstructural features being corrosion controlling factors in processes such as FSpJ [11] and  
469 Friction Stir Welding (FSW) [52-58].

470 The detailed analysis of **Fig. 8** suggests that for all the systems the localized corrosion attack in  
471 the nugget preferably occur at the heat affected zone (HAZ) and the outer edge of the thermo-  
472 mechanically affected zone (TMAZ).

473 This behavior is consistent with previous studies [36, 52, 57, 58], and can be attributed to a  
474 possible coarsening of the strengthening particles and an increase in the content of the Cu-rich  
475 second phases at the HAZ, due to the thermal cycle of the joining process. These particles being  
476 nobler, they promote the formation of localized galvanic cells and the anodic dissolution of the  
477 Al matrix. This has not been the case for the SZ, which shows more resistance to pitting  
478 corrosion although some discoloration can still be noticed. This fact can be linked to the  
479 significant heat and strain rate that this zone (SZ) underwent, thus leading to a redistribution

480 and decrease of the Cu-rich intermetallic content and favoring the creation of a native passive  
481 layer [36, 59].



482

483 **Fig. 8.** Photographs of the top surface of the bonding area with a) definition of the main  
484 microstructural zones produced by the FSpJ process on the AA2024-T3 part, b) reference without any  
485 treatment, c) treated with LDH-NO<sub>3</sub> and d) treated with LDH-VO<sub>x</sub>.

486

487 In spite of the corrosion degradation due to the process-related microstructural changes of  
488 AA2024-T3 and its intensification by the macro-galvanic corrosion (coupling with CF-PPS), a  
489 slight improvement can be visually observed with the samples treated with LDH-VO<sub>x</sub>. The  
490 latter samples show less pitting around the bonding area (**Fig. 8 d**).

491 Severe localized corrosion can be identified already after 3 weeks SST for the reference  
492 AA2024-T3. Overtime however, these localized dissolutions may also connect to create a  
493 network of larger pits [59].

494 Visually, no improvement toward weld nugget corrosion is observed for the AA2024-T3  
495 samples treated with LDH-NO<sub>3</sub>. Similarly to the observation of **Fig. 7**, it is apparent from the  
496 aspect of the top surface demonstrated in **Fig. 7 d**, that the LDH-VO<sub>x</sub> had a positive impact on  
497 the corrosion protection of the AA2024-T3. A few isolated pits can be observed after 3 weeks

498 SST and 6 weeks SST which were focused on the HAZ and outer edge of the TMAZ. It is  
499 reasonable to attribute the lack of corrosion protection in some of these isolated pits to a latent  
500 damage of the LDH layers, due to the pressure and mechanical input during the FSpJ process.

501

### 502 *3.3.2. Mechanical performance of joints*

503 After the surface examination of the metallic part of the joints, lap shear tensile test was utilized  
504 as the main method to assess the influence of the LDH conversion coatings on the  
505 mechanical/adhesion performance of the joints before and after 3- and 6-weeks exposure to  
506 SST. At least three specimens from each of the systems were tested to obtain average values  
507 that were put together in form of a statistical histogram (see **Fig. 9.**)

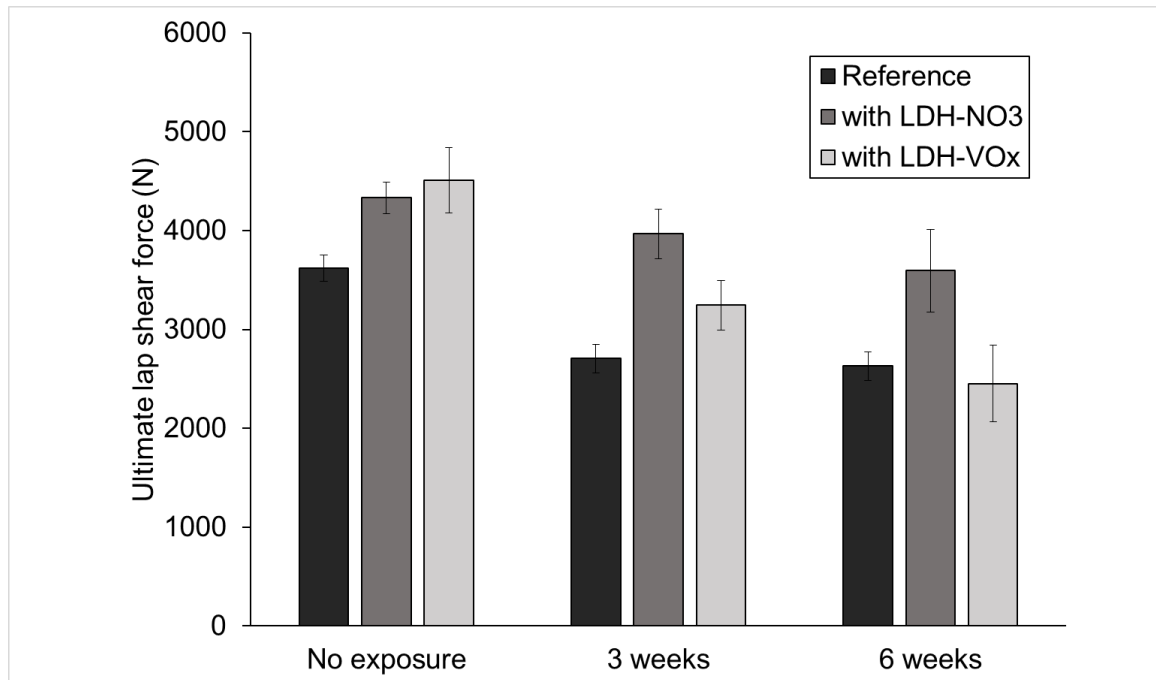
508 A clear improvement of the mechanical performance can be observed for the AA2024-T3-  
509 LDH-N/ CF-PPS and AA2024-T3-LDH-V/ CF-PPS joints in comparison to the reference joint.  
510 An increase of the ultimate lap shear force (ULSF) of about 19.66 % to 24.55 % (**Table. 1**) was  
511 achieved for AA2024-T3-LDH-N/CF-PPS and AA2024-T3-LDH-V/ CF-PPS, respectively  
512 before SST.

513 As it has already been established in previous studies [39], aluminum surface pre-treatment  
514 could have a significant impact on the final adhesion performance of the friction spot joints.  
515 The current findings are a first indication that the LDH pre-treatment on AA2024-T3 has a  
516 favorable effect on the adhesion forces of the metal-composite FSp joints.

517 After undergoing SST, the overall mechanical performance of the samples weakened. More  
518 importantly, the obtained results are partially contradictory to what has been concluded with  
519 the preliminary surface observation of the AA2024-T3 treated with LDH-NO<sub>3</sub> and LDH-VO<sub>x</sub>.  
520 In spite of well documented inhibition effect of vanadate [34-35, 46-47], the ZRA and SVET  
521 results shown above, the vanadate introduced into the LDH conversion layers does not impart  
522 a suppression of the corrosion induced disbonding.

523 The AA2024-T3-LDH-N/CF-PPS joint offered the best resistance towards corrosion in  
524 comparison to the reference joint and the AA2024-T3-LDH-V/ CF-PPS. While the AA2024-  
525 T3-LDH-N/CF-PPS maintained a good performance at the different steps of investigation, the  
526 mechanical (or adhesion) performance of the AA2024-T3-LDH-V/ CF-PPS dropped after 6  
527 weeks SST (**Table. 1**).

528



529  
 530 **Fig. 9.** Evolution of the average ULSF of the different FSp joints before SST and after 3- and 6 weeks  
 531 SST.  
 532

533 **Table. 1.** Percentage of improvement of the average ULSF in comparison to the reference joint  
 534 AA2024-T3/CF-PPS.

Samples	Before SST	3 weeks SST	6 weeks SST
LDH-NO <sub>3</sub>	19.66 %	42.79 %	36.75 %
LDH-VO <sub>x</sub>	24.55 %	16.79 %	- 6.75 %

535  
 536 The absence of the active protection by vanadate in the joint area can be related to its low  
 537 inhibition efficiency against galvanic corrosion as shown above. Presence of the vanadate was  
 538 even causing a deeper localized corrosion when AA2024 is coupled to CF-PPS. It can be stated  
 539 that the increased mechanical performance as well as the corrosion resistance of the specimens  
 540 with AA2024-T3-LDH-N, are mostly attributed to the structure of the LDH conversion coating  
 541 with a slight contribution of nitrate. The use of micro/nano scale structures such as LDH or  
 542 others clay fillers have already been exploited to reinforce the mechanical performance of some  
 543 organic coatings. They have proven to not interfere with the adhesion performance of the  
 544 coatings with the metallic substrate [60-63]. In addition to the hypothesis above, it is likely that  
 545 the PPS molten layer flowing into the asperities and irregularities at the surface of the AA2024-  
 546 T3, will attach easily to the surface due to the additional roughness generated by the LDH  
 547 conversion coating. Hence, the combination of the existing sandblasting treatment and the  
 548 formation of the LDH conversion coatings seems to enhance the micro-mechanical

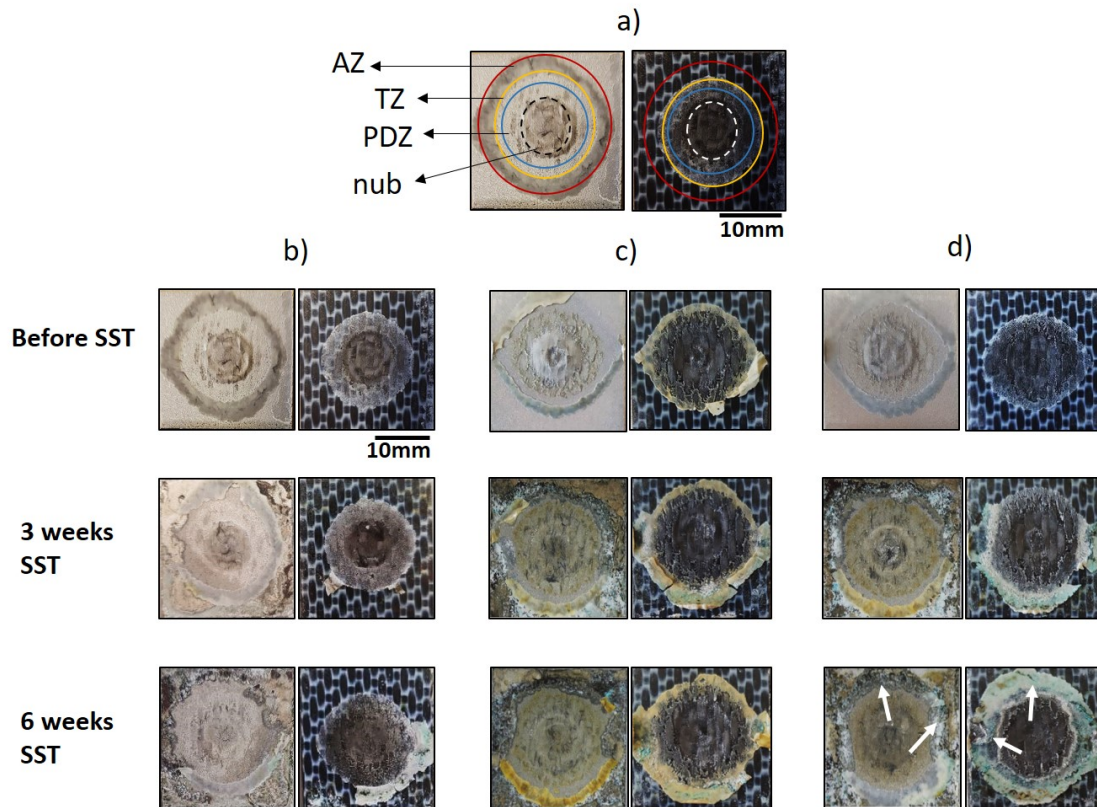
549 interlocking. Moreover, it is not the first time that surface treatments were claimed to reinforce  
550 the adhesion performance of hybrid joints. In the past, it has been proven that the formation of  
551 primary organic-metallic bonds between the composite and metallic parts, contribute greatly on  
552 the overall enhancement of the adhesion [64]. Therefore, in the case of the joint AA2024-T3-  
553 LDH-N/ CF-PPS the mechanical performance remained superior even after 6 weeks exposure  
554 to SST. Further investigations on the adhesion mechanisms should be performed to confirm  
555 these assumptions. Additionally, an active chloride trapping effect of LDH should not be  
556 excluded since it has been previously shown that LDH has the aptitude to uptake the  $Cl^-$  present  
557 at the surface while releasing the corrosion inhibitor [65].

558

### 559 **3.3.3. Failure analysis of the joint.**

560 In light of the promising mechanical results, it is worth having a closer look into the bonding  
561 area on both the AA2024-T3 and CF-PPS sides, after separation by tensile lap shear testing  
562 (**Fig. 10**).

563 The first photograph **Fig. 10 a** is an informative illustration delimiting the three main bonding  
564 zones previously defined in the literature [6] and known to the FSpJ process. Shortly, the first  
565 zone is called the Plastically Deformed Zone (PDZ) owing to the close contact between the  
566 polymer matrix and the carbon fibers with the plasticized aluminum. The PDZ includes also the  
567 metallic nub area. This zone is the strongest part of the joint. The outer region defined as the  
568 Adhesion Zone (AZ), is responsible for sealing the joint since it is where the molten polymer  
569 matrix is consolidated and adhesion forces are established. In between the PDZ and AZ regions,  
570 is a Transition Zone (TZ).



571

572 **Fig. 10.** Photographs of the bonding zone for the couple (metal part on the left and CF-PPS on the  
 573 right) after separation by lap shear tensile test with; a) delimitation of the borders between the main  
 574 regions defining the FSpJ process [39] ; b) the reference couple AA2024-T3/ CF-PPS, c) AA2024-T3-  
 575 LDH-N/ CF-PPS and d) AA2024-T3-LDH-V/ CF-PPS, before SST and after 3 and 6 weeks SST.

576

577 The effect of salt penetration between the two parts of the joints can be noticed for all treated  
 578 AA2024-T3 samples. The degradation due to corrosion is more noticeable outside the AZ  
 579 region of the AA2024-T3 since in this area the joints are not strongly attached.

580 For the purpose of comparing and evaluating which joints present better behavior toward  
 581 corrosion, the focus was given to the regions inside the AZ and PDZ. It is important to be able  
 582 to state in which circumstance the detachment was more relevant and possible penetration of  
 583 the salt through the consolidated polymer layer of AZ occurred.

584

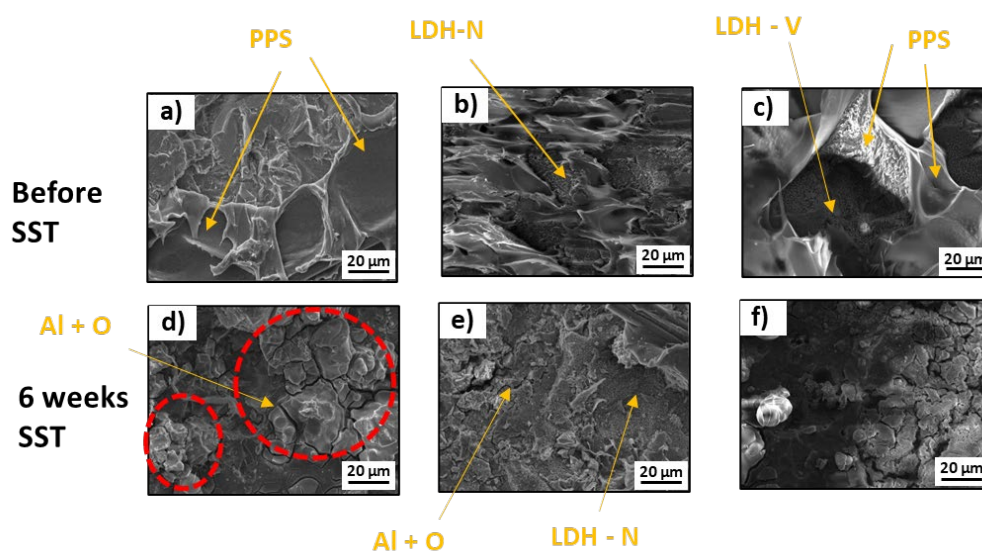
585 Overall, the area delimiting the AZ becomes smaller and the corrosion resistance decreases with  
 586 the increase of exposure time to SST. Nevertheless, looking carefully at the photographs of **Fig.**  
 587 **10 b-d**, the AA2024-T3 treated with LDH-NO<sub>3</sub> presents better resistance to corrosion in  
 588 comparison to the reference AA2024-T3 and the AA2024-T3 treated with LDH-VO<sub>x</sub>. In other  
 589 words, the polymer layer in the AZ appears to present better adhesion, and consequently offer

590 a more effective barrier to corrosion for the AA2024-T3 treated with LDH-NO<sub>3</sub>. This is an  
591 indication of the adhesion contribution of the LDH-NO<sub>3</sub> to the joint's interface.

592 As a result, superior mechanical properties after SST were revealed with the lap shear test for  
593 those joints. Moreover, looking at the AA2024-T3 samples treated with LDH-VO<sub>x</sub> (**Fig. 10 d**),  
594 the corrosion effect appears to be much pronounced with more corrosion products around the  
595 PDZ zone and with almost a non-existing AZ bordering zone after 6 weeks of SST (see white  
596 arrows on **Fig. 10 d**). Since the AZ represents an important protection barrier for the PDZ (most  
597 strong zone of the joints), its detachment from the aluminum surface due to corrosion leads to  
598 the deterioration of the core of the joint, and consequently lowering the mechanical properties  
599 [36].

600

601 An in-depth SEM coupled with EDS analysis of some of the images presented in **Fig. 10** was  
602 performed. **Fig. 11** shows the SEM images of an area from the PDZ or close to the PDZ of the  
603 AA2024-T3 part, before and after exposure to 6 weeks SST. More detailed SEM images of the  
604 different regions on the fraction analysis (on both AA2024-T3 and CF-PPS parts) are provided  
605 in the supplementary information (**Fig. S.5** to **Fig. S.11**).



606

607 **Fig. 11.** SEM fracture analysis of a region of the PDZ on the AA2024-T3 part of the joints with a)  
608 reference AA2024-T3, b) AA2024-T3-LDH-N, c) AA2024-T3-LDH-V before SST; and d) reference  
609 AA2024-T3, e) AA2024-T3-LDH-N and f) AA2024-T3-LDH-V after 6 weeks SST.

610

611 **Fig. 11 a** representing an area of the PDZ on the reference AA2024-T4, shows that it is almost  
612 completely covered by the polymer PPS. This is supported by the EDS analysis that indicated  
613 the presence of C and S elements (see arrows). A similar morphology can be observed on the  
614 AA2024-T3 samples treated with LDH-NO<sub>3</sub> and LDH-VO<sub>x</sub> (**Fig. 11 b** and **c**). However, the last

615 two SEM images also indicate the presence of the respective LDHs between the gap uncovered  
616 by PPS polymer (**Fig. 11 b** and **c**). This was confirmed by the detection of Al and Zn by EDS  
617 elemental analysis, in addition to N in the case of AA2024-T3-LDH-N and V in AA2024-T3-  
618 LDH-V, as indicated by the arrows.

619 The fraction analysis allowed to also observe one of the primary mechanisms of bonding based  
620 on the micro-mechanical interlocking achieved by the pull-off of the carbon fibers from the CF-  
621 PPS and their attachment on the metallic parts (see Fig. S.5 c from the supplementary  
622 information) [7, 66]. Moreover, it appears from the comparison of **Fig. 11 a-c** in addition to  
623 **Fig. S.5** to **Fig S. 7**, that LDH conversion coatings do not restrict the micro-mechanical  
624 interlocking between AA2024-T3 and CF-PPS to the PDZ. For instance, looking at **Fig. 11 c**,  
625 a tearing of the polymer as a result of the single lap shear test and the separation of the composite  
626 from the AA2024-T3 part can be observed. This tearing effect did not have a negative influence  
627 of the LDH layer, since the LDH-VO<sub>x</sub> remains attached to the Al substrate and a small amount  
628 stuck to the polymer. A higher magnification image of **Fig. 11 c** is provided separately in the  
629 supplementary material (**Fig. S.8**) with the results of the EDS analysis table.

630 Accordingly, the EDS analysis showed in **Fig. S.8** was aimed in two main areas; (1) represents  
631 a spot on the AA2024-T3 interface with LDH-VO<sub>x</sub> whereas (2) is a spot from the detached PPS  
632 polymer. The first spot is mainly enriched with the elements Al, Zn with a lower percentage of  
633 V, C and S. The first two elements confirm that the LDH film is rather resistant and do not  
634 detach from the interface easily while the latter two elements (C and S) indicate a remaining of  
635 PPS polymer at the interface. The second spot (2) is mainly enriched with C and S with  
636 negligible percentage of Al, Zn and V. Since these elements are associated to the composition  
637 of LDH-V, their absence on the detached polymer could mean that LDH do not adhere or is not  
638 compatible with the polymer. But this possibility can be certainly excluded due to the adhesion  
639 results demonstrated earlier with the lap shear test. Another explanation can be associated to  
640 the welding parameters in the sense that these were not optimal and the resin could not flow  
641 into the pores of the LDH layer.

642 After 6 weeks exposure to SST, corrosion degradation due to the penetration of the NaCl in  
643 between the joints had an important impact on the fracture images of the different joints. (See  
644 **Fig. 11 d-f** and **Fig. S.9** to **Fig. S. 11** from the supplementary material). The penetration of the  
645 NaCl solution into the joints lead to the deterioration of the AZ which is the main barrier against  
646 the advance of the aggressive species such as chlorides into the PDZ. In all AA2024-T3 parts  
647 regardless of the treatment, consolidated polymer around the AZ region was partly to  
648 completely (AA2024-T3-LDH-V) detached from the AA2024-T3 interface, followed by further

649 penetration of the salts into the PDZ area and the advance of the corrosion degradation. This  
650 will lead to the shortening of ration of unaffected PDZ area, as shown previously in **Fig. 10**.  
651 The formation of a dome of hydrated aluminum oxides (circled in red in **Fig. 11 d**) is a result  
652 of the contact of the acidic anolyte solution carrying the dissolved Al cations with a solution  
653 which has a higher pH probably generated from local cathodic oxygen reduction [50, 67].  
654 Moreover, since a high signal of Cu is found in these regions (**Fig. S.9 e**), it was assumed in  
655 previous studies to be a consequence of the S-phase dealloying process [67].  
656 Aside from the presence of LDH with the respective anions, similar deductions in regards to  
657 the corrosion tendency can be achieved when looking at the AA2024-T3 treated with LDH-  
658 NO<sub>3</sub> (**Fig. 11 e**) and LDH-VO<sub>x</sub> (**Fig. 11 f**). The appearance of the AA2024-T3-LDH-N surface  
659 seems less damaged in comparison to the reference AA2024-T3 without any treatment (**Fig. 11**  
660 **e**). Nevertheless, the inspection of few areas of the overall surface is not enough to make a full  
661 conclusion on the corrosion improvement.

662

#### 663 **IV. Discussion**

664 Looking into the assembled results starting from the EDS fracture analysis of the AA2024-T3-  
665 LDH-V/CF-PPS, it is interesting to notice that the regions where EDS detected a high signal of  
666 Cu were overlapped with a strong signal of the element V. This implies that the corrosion  
667 inhibitor vanadate may play a role on impeding the cathodic oxygen reduction taking place at  
668 active sites (Cu-rich intermetallic). These findings are in a good agreement with the literature  
669 [46, 52].

670 Although the above supposition proves that vanadate participated in the reactions taking place  
671 at the interface, the extent or nature of its role in terms of inhibition or acceleration of corrosion  
672 remains complex, seeing that the data disclosed in **Fig. 9** and **Table 1** portray an unfavorable  
673 joint mechanical performance.

674 The nature of the environment that vanadate was subjected to, could have significantly  
675 influenced its speciation. The V-species hosted between the LDH interlayers and confined to  
676 the area of joining with CF-PPS may react differently as they would have on an open  
677 environment outside the bonding zone. Indeed, an obvious improvement of corrosion at the  
678 surface of the metal was noted for the AA2024-T3-LDH-V, whereas evidence of corrosion was  
679 seen for the reference alloy and the one with AA2024-T3-LDH-N (**Fig. 7**). However, the  
680 situation was completely different at the close vicinity between CF-PPS and AA2024 (**Fig. 9**)  
681 and examining the fractured parts (**Fig. 11**).

682 Several interpretations to the mechanism of inhibition of vanadate for Al alloys can be found  
683 in the literature [46-47, 68-70]. As an attempt to understand what happened in the course of this  
684 study and make a link with the previous findings, Raman spectroscopy was used to first identify  
685 the existing vanadate species at different stages of the investigation.

686 **Fig. S.12** depicts three Raman spectra collected on the AA2024-T3-LDH-V part : a) before  
687 exposure to SST and joining with CF-PPS (**Fig. S.12 a**), b) after 6 weeks SST and separation  
688 from the CF-PPS with a focus on the PDZ zone (**Fig. S.12 b**) and, c) outside the bonding area  
689 (**Fig. S.12 c**).

690 The Raman spectra of the AA2024-T3-LDH-V samples before SST (**Fig. S.12 a**) presents a  
691 strong bands at around  $355\text{ cm}^{-1}$  that is assigned to the bending mode (V=O) of the V-Species  
692 with the formula  $(\text{VO}_3)_n^{n-}$  [71], and a broad band between  $700$  and  $1000\text{ cm}^{-1}$  with a sharp end  
693 at  $944\text{ cm}^{-1}$ . This is attributed to the V-O-V stretching vibration of the monovanadate species and  
694 different oligomers among which are: divanadates ( $\text{V}_2$ ) and forward, with the predominance of  
695 decavanadate ( $\text{V}_{10}$ ) with the formula  $\text{V}_4\text{O}_{12}^{4-}$  at  $944\text{ cm}^{-1}$  [63, 65-66]. Monovanadate has been  
696 shown to present efficient corrosion inhibition properties whereas decavanadate presents a poor  
697 inhibition efficiency [46].

698 After 6 weeks SST and separation of the joints (**Fig. S.12 b**), the Raman spectra of a point  
699 measurement performed at the PDZ zone revealed a strong band at around  $1075\text{ cm}^{-1}$ , the  
700 assignment of this band it is not certain but according to the work of B.L. Hurley, S. Qiu, R. G.  
701 Buchheit [69] , the terminal V=O bond for monovanadate appear around this region. Another  
702 relevant wavelength appears at around  $1180\text{ cm}^{-1}$ , and this is a characteristic band of  
703 polyphenylene sulfide (PPS) [73].

704 Among some of the already identified band, one interesting large band at  $850-900$  emerges on  
705 the last spectra collected outside the bonding area after 6 weeks SST (**Fig. S.12 c**). A sharp  
706 ending to the band can be identified at approx.  $869\text{ cm}^{-1}$ . The thorough Raman investigation of  
707 aqueous vanadate species and their interaction with AA2024-T3 carried out by B.L. Hurley, S.  
708 Qiu and R.G. Buchheit [69] assigned the band in the range of  $850-865$  to the V=O stretch in  
709  $\text{Cu}_3(\text{VO}_4)_2$ , which is of particular importance since it confirms the interaction of the vanadate  
710 inhibitor with the Cu-rich intermetallic. Hence, verifying the localized inhibition mechanism of  
711 vanadate. A summary of the mentioned wavenumbers is listed in **Table. S.1**.

712 Based on the above analysis, it can be concluded that the Raman signal for V-species at the  
713 PDZ area is very limited. The reason could be either due to the surface being covered by the  
714 molten PPS or that the signals referring to the presence of the V-species that play a role for  
715 corrosion inhibition are almost non-existent.

716 It appears that the inhibitive actions of vanadate happened at the interface of the AA2024-T3  
717 outside the bonding area of the joint and similar mechanism was observed for the systems  
718 analyzed with SVET. The conditions in the later cases are very similar and coincide with the  
719 conclusions achieved in other works [46, 68-69]. According to Ralston et al. [68], the vanadate  
720 action manifest by a formation of localized film over the AA2024-T3 matrix. In certain  
721 instances, it is not evident to detect the segregation of vanadium and confirm the thin layer  
722 formation. Although, the vanadate film formation does not depend on the aeration but it is  
723 highly contingent to the change of pH. Besides, J. Li, B. Hurley, R.G. Buchheit [51] claimed  
724 that at  $T < 50^{\circ}\text{C}$  the film is mainly identified on the intermetallic and very little on the matrix.  
725 The authors also found that in the presence of  $\text{NaVO}_3$  solution, the S-phase dealloying was  
726 significantly reduced.

727 Reasoning from this fact, a meaningful change on the environment such as the exposition to a  
728 closed area after joining with CF-PPS by FSpJ may have affected the behavior of the vanadate  
729 (e.g. pH changes to an influence from the molten PPS). In addition, it has been claimed that  
730 galvanic corrosion is a process that can be unique to each couple as well as to the factors  
731 governing the surrounding environment, therefore the electrochemical properties can be very  
732 distinctive from one environment to another [74] and this assumption extends to the interaction  
733 of inhibitors such as vanadate to the corresponding environment.

734 Despite the poor performance demonstrated by the LDH intercalated with vanadate, this does  
735 not mean that the nature of LDH conversion coating used in this study are ineffective in  
736 improving the mechanical and corrosion resistance properties of FSp joint. The LDH layer with  
737 nitrate anions contributed significantly in maintaining the stability of the joints in the corrosive  
738 environment as well as increasing the mechanical performance. Due to its relatively low  
739 affinity, nitrate could be easily exchanged with the anions present in the environment [75]. For  
740 instance, nitrate can be exchange with the aggressive chloride anions present in between the  
741 joints which would prevent further corrosion attack of the latter anion on the AA2024-T3 part.  
742 This nano-trapping property of LDH has been previously reported as a mechanism of action of  
743 the LDH on the corrosion prevention in Al alloy [65]. It is very possible that in this current  
744 work, the nano-trapping properties of LDH and the slight inhibitive action of the nitrate anions  
745 [35] were enough to assure an effective corrosion resistance of the joints.

746

747 In summary, the LDH nanocontainer as a conversion layer has proven to be beneficial to the  
748 overall corrosion protection of the joints without compromising their mechanical properties.  
749 However, using a known and strong corrosion inhibitor such as vanadate may not always be

750 the best solution. One may think of exploiting the anion-exchange ability of the LDH  
751 nanocontainer for its nano-trapping advantage rather than just its capacity to store corrosion  
752 inhibitors. Moreover, this work was proof of concept in the sense that it shows that the  
753 application of LDH conversion coatings can be extended to the welded joints specifically hybrid  
754 joints.

755

## 756 **V. Conclusions**

757 A pre-treatment of AA2024-T3 based on LDH conversion coatings was introduced as a step  
758 before the Friction Spot Joining process with CF-PPS. The idea is to reduce the overall galvanic  
759 corrosion effect of the joints without interfering with their mechanical performance. In addition,  
760 vanadate was used as model corrosion inhibitor to be intercalated between the LDH interlayers.  
761 By means of different investigating methods, a comprehensive evaluation of the joints was  
762 achieved and the following points were made:

763 1. The joints adhesion performance was increased by above 20 % after treatment of  
764 AA2024 with LDH conversion coatings.

765 2. LDH conversion treatment decreases the corrosion induced degradation of the joint. The  
766 joint subjected to a treatment with LDH-NO<sub>3</sub> presented superior mechanical  
767 performance (approx. 37 %) in comparison to the reference joint after 6 weeks of salt  
768 spray test. This could be associated more to the nano-trapping property of the LDH  
769 rather to a corrosion inhibition effect.

770 3. The treatment of AA2024 with LDH-VO<sub>x</sub> did not reveal any positive effect in terms of  
771 delayed corrosive degradation of the joint. However, this is due to the behavior of  
772 vanadate as a corrosion inhibitor rather than the nature of the LDH conversion coating.  
773 The labile nature of vanadate speciation at different conditions (pH, electrochemical  
774 potential) could be responsible for such poor performance.

775 Finally, the combination of sandblasting and LDH treatment helped reinforce both mechanical  
776 performance and corrosion resistance of the joints. However, it would be beneficial in the future  
777 to perform a systematic study and scan several inhibiting systems that could be efficient in  
778 tackling the galvanic effect in CFRP/Al alloys systems. Moreover, these selected inhibitors  
779 should be able to withstand the conditions of the welding process and be stable in confined  
780 environments such as the interface between the Al alloy and CFRP parts.

781

782

## 783 **Acknowledgements**

784 This work was realized thanks to a partial financial support from European FP7 project  
785 “PROAIR” (PIAPP-GA-2013-612415) and Horizon 2020 project “MULTISURF” (Marie  
786 Skłodowska-Curie grant agreement No 645676).

787 A.C. Bouali thanks the DAAD financial support in the form of an International Travel Grant,  
788 which enabled her to attend the International Conference on Surface Modification Technologies  
789 33 (SMT-33) and present this work.

790 N.M. André would like to acknowledge the support of the National Council for Scientific and  
791 Technological Development (CNPq Brazil, Process 200694/2015-4).

792 S.T. Amancio-Filho would like to acknowledge the financial support from the Austrian aviation  
793 program “TAKE-OFF” and from the Austrian Ministry for Climate Action, Environment,  
794 Energy, Mobility, Innovation and Technology, BMK.

795

796 **Declarations of interest:** No competing interests can be declared.

797

798 **Data availability:** The raw/processed data required to reproduce these findings cannot be  
799 shared at this time as the data also forms part of an ongoing study.

800

## 801 **References**

802 [1] NACE, Galvanic Corrosion. [https://www.nace.org/resources/general-resources/corrosion-](https://www.nace.org/resources/general-resources/corrosion-basics/group-1/galvanic-corrosion)  
803 [basics/group-1/galvanic-corrosion](https://www.nace.org/resources/general-resources/corrosion-basics/group-1/galvanic-corrosion) (accessed 24 July 2019).

804 [2] C. Soutis, Fibre reinforced composites in aircraft construction, *Prog. Aerosp. Sci.* 41 (2005)  
805 143-151.

806 [3] C. Vargel, *Corrosion of aluminium*, Elsevier, 2004.

807 [4] R. Srinivasan, J.A. Nelson, L.H. Hihara, Development of guidelines to attenuate galvanic  
808 corrosion between mechanically-coupled aluminum and carbon-fiber reinforced epoxy  
809 composites using insulation layers, *J. Electrochem. Soc.* 162 (2015) C545-C554.

810 [5] Y. Huang, X. Meng, Y. Xie, L. Wan, Z. Lv, J. Cao, J. Feng, Friction stir welding/processing  
811 of polymers and polymer matrix composites, *Compos. Part A Appl. Sci. Manuf.* 105 (2018)  
812 235-257.

813 [6] S. Goushegir, J. Dos Santos, S. Amancio-Filho, Friction spot joining of aluminum  
814 AA2024/carbon-fiber reinforced poly (phenylene sulfide) composite single lap joints:  
815 microstructure and mechanical performance, *Mater. Des.* 54 (2014) 196-206.

816 [7] N. Manente André, J. F dos Santos, S. T Amancio-Filho, Evaluation of Joint Formation and  
817 Mechanical Performance of the AA7075-T6/CFRP Spot Joints Produced by Frictional Heat,  
818 *Materials*, 12 (2019) 891.

819 [8] X. Meng, Y. Huang, Y. Xie, J. Li, M. Guan, L. Wan, Z. Dong, J. Cao, Friction self-riveting  
820 welding between polymer matrix composites and metals. *Compos. Part A Appl. Sci. Manuf.*  
821 127 (2019), 105624.

822 [9] Y. Huang, X. Meng, Y. Xie, J. Li, L. Wan, Joining of carbon fiber reinforced thermoplastic  
823 and metal via friction stir welding with co-controlling shape and performance, *Compos. Part*  
824 *A Appl. Sci. Manuf.* 112 (2018), 328-336.

825 [10] S.M. Goushegir, N. Scharnagl, J.F. dos Santos, S.T. Amancio-Filho, Durability of Metal-  
826 Composite Friction Spot Joints under Environmental Conditions, *Materials*. 13 (2020) 1144.

827 [11] N. M. André, S.M. Goushegir, N. Scharnagl, J.F. dos Santos, L.B. Canto, S.T. Amancio-  
828 Filho, Composite surface pre-treatments: Improvement on adhesion mechanisms and  
829 mechanical performance of metal–composite friction spot joints with additional film interlayer,  
830 *J. Adhes.* 94 (2018) 723-742.

831 [12] S.C. Han, L.H. Wu, C.Y. Jiang, N. Li, C. L. Jia, P. Xue, H. Zhang, H.B. Zhao, D.R. Ni,  
832 B.L. Xiao, Z.Y. Ma, Achieving a strong polypropylene/aluminum alloy friction spot joint via a  
833 surface laser processing pretreatment, *J. Mater. Sci. Technol.* 50 (2020) 103-114.

834 [13] F.C. Liu, J. Liao, Y. Gao, K. Nakata, Effect of plasma electrolytic oxidation coating on  
835 joining metal to plastic, *Sci. Technol. Weld. Joi.* 20 (2015), 291-296.

836 [14] F. Bellucci, Galvanic corrosion between nonmetallic composites and metals II. Effect of  
837 area ratio and environmental degradation, *Corrosion*. 48 (1992) 281-291.

838 [15] S. Palani, T. Hack, A. Peratta, R. Adey, J. Baynham, H. Lohner, Modelling approach for  
839 galvanic corrosion protection of multi-material aircraft structures, in: *Proc. DoD Corrosion*  
840 *Conference 2011*, 2011.

841 [16] S. Kallip, A.C. Bastos, K.A. Yasakau, M.L. Zheludkevich, M.G.S. Ferreira, Synergistic  
842 corrosion inhibition on galvanically coupled metallic materials, *Electrochem. Commun.* 20  
843 (2012) 101-104.

844 [17] M. Serdechnova, S. Kallip, M.G.S. Ferreira, M.L. Zheludkevich, Active self-healing  
845 coating for galvanically coupled multi-material assemblies. *Electrochem. Commun.* 41 (2014)  
846 51-54.

847 [18] R. Ireland, L. Arronche, V. La Saponara, Electrochemical investigation of galvanic  
848 corrosion between aluminum 7075 and glass fiber/epoxy composites modified with carbon  
849 nanotubes, *Composites Part B: Engineering*. 43 (2012) 183-194.

850 [19] M. Mandel, L. Krüger, Determination of pitting sensitivity of the aluminium alloy EN  
851 AW-6060-T6 in a carbon-fibre reinforced plastic/aluminium rivet joint by finite element  
852 simulation of the galvanic corrosion process, *Corr. Sci.* 73 (2013) 172-180

853 [20] Z. Liu, M. Curioni, P. Jamshidi, A. Walker, P. Prengnell, G. Thompson, P. Skeldon,  
854 Electrochemical characteristics of a carbon fibre composite and the associated galvanic effects  
855 with aluminium alloys, *Appl. Surf. Sci.* 314 (2014) 233-240.

856 [21] E. Håkansson, J. Hoffman, P. Predecki, M. Kumosa, The role of corrosion product  
857 deposition in galvanic corrosion of aluminum/carbon systems, *Corr.Sci.* 114 (2017) 10-16.

858 [22] L. Pan, W. Ding, W. Ma, J. Hu, X. Pang, F. Wang, J. Tao, Galvanic corrosion protection  
859 and durability of polyaniline-reinforced epoxy adhesive for bond-riveted joints in  
860 AA5083/Cf/Epoxy laminates, *Mater. Des.* 160 (2018) 1106-1116.

861 [23] L.B. Coelho, M. Mouanga, M.E. Druart, L. Recloux, M.G. Olivier, A SVET study of the  
862 inhibitive effects of benzotriazole and cerium chloride solely and combined on an  
863 aluminium/copper galvanic coupling model, *Corr. Sci.* 110 (2016) 143-156.

864 [24] L.B. Coelho, M. Taryba, M. Alves, X. Noirfalise, M.F. Montemor, M.G. Olivier, The  
865 corrosion inhibition mechanisms of Ce (III) ions and triethanolamine on graphite—AA2024-  
866 T3 galvanic couples revealed by localised electrochemical techniques, *Corr. Sci.* 150 (2019)  
867 207-217.

868 [25] M. Oliveira, A.C. Bastos, S. Kallip, T. Hack, M.L. Zheludkevich, M.G.S. Ferreira,  
869 Corrosion Inhibition and Acceleration by Rare Earth Ions in Galvanic Couples, *J. Electrochem.*  
870 *Soc.* 166 (2019) C642-C648.

871 [26] E. Shchukina, H. Wang, D.G. Shchukin, Nanocontainer-based self-healing coatings:  
872 current progress and future perspectives, *Chem. Commun.* 55 (2019) 3859-3867.

873 [27] M.L. Zheludkevich, J. Tedim, and M.G.S. Ferreira, “Smart” coatings for active corrosion  
874 protection based on multi-functional micro and nanocontainers, *Electrochim. Acta.* 82 (2012)  
875 p. 314-323.

876 [28] J. Tedim, M. Zheludkevich, A. Salak, A. Lisenkov, M.G.S. Ferreira, Nanostructured LDH-  
877 container layer with active protection functionality, *J. Mater. Chem.* 21 (2011) 15464-15470.

878 [29] A. Gomes, D. Cocke, D. Tran, A. Bakshi, Layered double hydroxides in energy research:  
879 advantages and challenges, in: *Energy Technology 2015*, Springer, 2015, pp. 309-316.

880 [30] X. Guo, F. Zhang, D.G. Evans, X.J.C.C. Duan, Layered double hydroxide films: synthesis,  
881 properties and applications, *Chem. Commun.* 46 (2010) 5197-5210.

882 [31] X. Duan, D.G. Evans, Layered double hydroxides, Springer Science & Business Media,  
883 2006.

884 [32] D.G. Evans, R.C. Slade, Structural aspects of layered double hydroxides, in: Layered  
885 double hydroxides, Springer, 2006, pp. 1-87.

886 [33] F. Zhang, L. Zhao, H. Chen, S. Xu, D.G. Evans, X.J.A.C. Duan, Corrosion resistance of  
887 superhydrophobic layered double hydroxide films on aluminum, *Angewandte Chemie*  
888 *International Edition*, 47 (2008) 2500-2503.

889 [34] J. Tedim, M. Zheludkevich, A. Bastos, A. Salak, A. Lisenkov, M.G.S. Ferreira, Influence  
890 of preparation conditions of layered double hydroxide conversion films on corrosion protection,  
891 *Electrochim. Acta.* 117 (2014) 164-171.

892 [35] J. Tedim, A. Bastos, S. Kallip, M. Zheludkevich, M.G.S. Ferreira, Corrosion protection of  
893 AA2024-T3 by LDH conversion films. Analysis of SVET results, *Electrochim. Acta.* 210  
894 (2016) 215-224.

895 [36] N.M. André, A. Bouali, E. Maawad, P. Staron, J.F. Santos, M.L. Zheludkevich, S.T.  
896 Amancio-Filho, Corrosion behavior of metal-composite hybrid joints: Influence of  
897 precipitation state and bonding zones, *Corr. Sci.* 158 (2019) 108075.

898 [37] Aluminium AA2024-T3 technical data sheet, in: Constellium (Ed.), France, 2012.

899 [38] CETEX® PPS technical datasheet, in: T.A. Composites (Ed.), Netherlands 2009.

900 [39] S.M. Goushegir, Friction spot joining of metal-composite hybrid structures, Helmholtz-  
901 Zentrum Geesthacht, Zentrum für Material-und Küstenforschung GmbH, 2015.

902 [40] S.M. Goushegir, J.F. dos Santos, S.T. Amancio-Filho, Influence of aluminum surface pre-  
903 treatments on the bonding mechanisms and mechanical performance of metal-composite single-  
904 lap joints, *Weld World* 2017.

905 [41] A.C. Bouali, A.C. Bastos, S.V. Lamaka, M. Serdechnova, M.G.S. Ferreira, M.L.  
906 Zheludkevich, Evaporation of Electrolyte During SVET Measurements: The Scale of the  
907 Problem and the Solutions, *Electroanalysis.* 31 (2019) 1-10.

908 [42] E.M. Seftel, E. Popovici, M. Mertens, K. De Witte, G. Van Tendeloo, P. Cool, E.F.  
909 Vansant, M. Materials, Zn-Al layered double hydroxides: synthesis, characterization and  
910 photocatalytic application, *Micropor. Mesopor. Mat.* 113 (2008) 296-304.

911 [43] K. Nejati, A.R. Akbari, S. Davari, K. Asadpour-Zeynali, Z. Rezvani, Zn-Fe-layered double  
912 hydroxide intercalated with vanadate and molybdate anions for electrocatalytic water oxidation,  
913 *New J. Chem.* 42 (2018) 2889-2895.

914 [44] M. Serdechnova, A.N. Salak, F.S. Barbosa, D.E. Vieira, J. Tedim, M.L. Zheludkevich,  
915 M.G.S. Ferreira, Interlayer intercalation and arrangement of 2-mercaptobenzothiazolate and 1,  
916 2, 3-benzotriazolite anions in layered double hydroxides: in situ X-ray diffraction study, *J.*  
917 *Solid. State. Chem.* 233 (2016) 158-165.

918 [45] L. Yang, A.A. Yang, Communication—On Zero-Resistance Ammeter and Zero-Voltage  
919 Ammeter, *J. Electrochem. Soc.* 164 (2017) C819-C821.

920 [46] M. Iannuzzi, G.S. Frankel, Mechanisms of corrosion inhibition of AA2024-T3 by  
921 vanadates, *Corr. Sci.* 49 (2007) 2371-2391.

922 [47] D.S. Kharitonov, C. Örnek, P.M. Claesson, J. Sommertune, I.M. Zharskii, I.I. Kurilo, J.  
923 Pan, Corrosion inhibition of aluminum alloy AA6063-T5 by Vanadates: microstructure  
924 characterization and corrosion analysis, *J. Electrochem. Soc.* 165 (2018) C116-C126.

925 [48] A.C. Bastos, M.C. Quevedo, O.V. Karavai, M.G.S. Ferreira, on the application of the  
926 scanning vibrating electrode technique (SVET) to corrosion research, *J. Electrochem. Soc.* 164  
927 (2017) C973-C990.

928 [49] T. Hu, H. Shi, D. Hou, T. Wei, S. Fan, F. Liu, E.H. Han, A localized approach to study  
929 corrosion inhibition of intermetallic phases of AA 2024-T3 by cerium malate, *Appl. Surf. Sci.*  
930 467 (2019) 1011-1032.

931 [50] A. Boag, A. Hughes, A. Glenn, T. Muster, D. McCulloch, Corrosion of AA2024-T3 Part  
932 I: Localised corrosion of isolated IM particles, *Corr. Sci.* 53 (2011) 17-26.

933 [51] J. Li, B. Hurley, R. Buchheit, Inhibition performance study of vanadate on AA2024-T3 at  
934 high temperature by SEM, FIB, Raman and XPS, *J. Electrochem. Soc.* 162 (2015) C219-C227.

935 [52] S.K. Ales, L. Wang, Effects of Friction Stir Welding on Corrosion Behaviors of AA2024-  
936 T4 Aluminum Alloy, in: *MATEC Web of Conferences*, EDP Sciences, 2017, pp. 02003.

937 [53] R. Fonda, P. Pao, H. Jones, C. Feng, B. Connolly, A. Davenport, Microstructure,  
938 mechanical properties, and corrosion of friction stir welded Al 5456, *Materials Science and*  
939 *Engineering: A*, 519 (2009) 1-8.

940 [54] O. Hatamleh, P.M. Singh, H. Garmestani, Corrosion susceptibility of peened friction stir  
941 welded 7075 aluminum alloy joints, *Corr. Sci.* 51 (2009) 135-143.

942 [55] J. Kang, R. D. Fu, G.H. Luan, C.L. Dong, M. He, In-situ investigation on the pitting  
943 corrosion behavior of friction stir welded joint of AA2024-T3 aluminium alloy, *Corr.Sci.* 52  
944 (2010) 620-626.

945 [56] J. Lumsden, M. Mahoney, G. Pollock, C. Rhodes, Intergranular corrosion following  
946 friction stir welding of aluminum alloy 7075-T651, *Corrosion*, 55 (1999) 1127-1135.

947 [57] M. Jariyaboon, A. Davenport, R. Ambat, B. Connolly, S. Williams, D. Price, The effect of  
948 welding parameters on the corrosion behaviour of friction stir welded AA2024-T351, *Corr.*  
949 *Sci.* 49 (2007) 877-909.

950 [58] C. Paglia, M. Carroll, B. Pitts, T. Reynolds, R. Buchheit, Strength, corrosion and  
951 environmentally assisted cracking of a 7075-T6 friction stir weld, in: *Materials Science Forum*,  
952 *Trans Tech Publ*, 2002, pp. 1677-1684.

953 [59] F. Gharavi, K.A. Matori, R. Yunus, N.K. Othman, Investigation of the nugget zone  
954 corrosion behavior in friction stir welded lap joints of 6061-T6 aluminum alloy, *Materials*  
955 *Research*, 17 (2014) 1563-1574.

956 [60] M. Bagherzadeh, F. Mahdavi, Preparation of epoxy–clay nanocomposite and investigation  
957 on its anti-corrosive behavior in epoxy coating, *Prog. Org. Coat.* 60 (2007) 117-120.

958 [61] A.H. Navarchian, M. Joulazadeh, F. Karimi, Investigation of corrosion protection  
959 performance of epoxy coatings modified by polyaniline/clay nanocomposites on steel surfaces,  
960 *Prog. Org. Coat.* 77 (2014) 347-353.

961 [62] N. Relosi, O.A. Neuwald, A.J. Zattera, D. Piazza, S.R. Kunst, E.J. Birriel, Effect of  
962 addition of clay minerals on the properties of epoxy/polyester powder coatings, *Polímeros*, 28  
963 (2018) 355-367.

964 [63] S. Chhetri, P. Samanta, N.C. Murmu, T. Kuila, Anticorrosion Properties of Epoxy  
965 Composite Coating Reinforced by Molybdate-Intercalated Functionalized Layered Double  
966 Hydroxide, *J. Compos. Sci.* 3 (2019) 11.

967 [64] S. M. Goushegir, N. Scharnagl, J. F. dos Santos, S.T. Amancio-Filho, XPS analysis of the  
968 interface between AA2024-T3/CF-PPS friction spot joints, *Surf. Interface. Anal.* 48 (2016)  
969 706-711.

970 [65] J. Tedim, A. Kuznetsova, A.N. Salak, F. Montemor, D. Snihirova, M. Pilz, M.L.  
971 Zheludkevich, M.G.S. Ferreira, Zn–Al layered double hydroxides as chloride nanotraps in  
972 active protective coatings, *Corr. Sci.* 55 (2012) 1-4.

973 [66] F. Balle, G. Wagner, D. Eifler, Ultrasonic spot welding of aluminum sheet/carbon fiber  
974 reinforced polymer–joints, *Materialwissenschaft und Werkstofftechnik: Entwicklung,*  
975 *Fertigung, Prüfung, Eigenschaften und Anwendungen technischer Werkstoffe*, 38 (2007) 934-  
976 938.

977 [67] A. Hughes, A. Boag, A. Glenn, D. McCulloch, T. Muster, C. Ryan, C. Luo, X. Zhou, G.  
978 Thompson, Corrosion of AA2024-T3 Part II: Co-operative corrosion, *Corr. Sci.* 53 (2011) 27-  
979 39.

980 [68] K. Ralston, S. Chrisanti, T. Young, R. Buchheit, Corrosion inhibition of aluminum alloy  
981 2024-T3 by aqueous vanadium species, *J. Electrochem. Soc.* 155 (2008) C350-C359.

- 982 [69] B.L. Hurley, S. Qiu, R. Buchheit, Raman spectroscopy characterization of aqueous  
983 vanadate species interaction with aluminum alloy 2024-T3 surfaces, *J. Electrochem. Soc.* 158  
984 (2011) C125-C131.
- 985 [70] Y. Li, S. Li, Y. Zhang, M. Yu, J. Liu, Enhanced protective Zn–Al layered double hydroxide  
986 film fabricated on anodized 2198 aluminum alloy, *J. Alloys Compd.* 630 (2015) 29-36.
- 987 [71] I.D. Dobrea, C.E. Ciocan, E. Dumitriu, M.I. Popa, E. Petit, V. Hulea, Raman  
988 spectroscopy—Useful tool for studying the catalysts derived from Mo and V-oxyanion-  
989 intercalated layered double hydroxides, *Appl. Clay. Sci.* 104 (2015) 205-210.
- 990 [72] D. Mata, M. Serdechnova, M. Mohedano, C. Mendis, S. Lamaka, J. Tedim, T. Hack, S.  
991 Nixon, M. Zheludkevich, Hierarchically organized Li–Al-LDH nano-flakes: a low-temperature  
992 approach to seal porous anodic oxide on aluminum alloys, *RSC. Adv.* 7 (2017) 35357-35367.
- 993 [73] D.A. Zimmerman, J.L. Koenig, H. Ishida, Infrared and Raman spectroscopy of cyclohexa  
994 (p-phenylene sulfide) and the polymer obtained therefrom, *Polymer*, 40 (1999) 4723-4731.
- 995 [74] X. Zhang, Galvanic corrosion, *Uhlig's Corrosion Handbook*, 51 (2011) 123.
- 996 [75] S. Miyata, Anion-exchange properties of hydrotalcite-like compounds, *Clays. Clay.*  
997 *Miner.* 31 (1983) 305-311.